The way we measure: comparison of methods to derive radial surface brightness profiles

Peters, S. P. C.; van der Kruit, P. C.; de Jong, R. S.

Published in:
Monthly Notices of the Royal Astronomical Society

DOI:
10.1093/mnras/stw2404

Publication date:
2017

Monthly Notices
of the
ROYAL ASTRONOMICAL SOCIETY

MNRAS **464,** 1591–1606 (2017)
Advance Access publication 2016 September 22

doi:10.1093/mnras/stw2404

The way we measure: comparison of methods to derive radial surface brightness profiles

S. P. C. Peters,[1] P. C. van der Kruit[1]★ and R. S. de Jong[2]

[1] *Kapteyn Astronomical Institute, University of Groningen, P.O.Box 800, NL-9700 AV Groningen, the Netherlands*
[2] *Leibniz Institut für Astrophysik Potsdam (AIP), An der Sternwarte 16, D-14482 Potsdam, Germany*

Accepted 2016 September 21. Received 2016 September 19; in original form 2015 July 23

ABSTRACT

The breaks and truncations in the luminosity profile of face-on spiral galaxies offer valuable insights in their formation history. The traditional method of deriving the surface photometry profile for face-on galaxies is to use elliptical averaging. In this paper, we explore the question whether elliptical averaging is the best way to do this. We apply two additional surface photometry methods, one new: principal axis summation, and one old that has become seldom used: equivalent profiles. These are compared to elliptically averaged profiles using a set of 29 face-on galaxies. We find that the equivalent profiles match extremely well with elliptically averaged profiles, confirming the validity of using elliptical averaging. The principal axis summation offers a better comparison to edge-on galaxies.

Key words: galaxies: photometry – galaxies: spiral – galaxies: structure.

1 INTRODUCTION

The surface photometry of a galaxy is the relationship of the radius R, seen from the centre of a galaxy, with the surface brightness $\mu(R)$. To first order, light traces mass in a galaxy. It is therefore an interesting tool for the study of galaxy dynamics and evolution. The first studies on the subject are by Patterson (1940) and de Vaucouleurs (1948, 1959), who noted that the surface brightness of the disc of spiral galaxies followed an exponential decline. The exponential nature was studied in more detail by Freeman (1970), who found that there was a second type of profiles that exhibits a break, beyond which the brightness decreases more rapidly.

The lines of sight in an edge-on galaxy are typically longer than in a face-on galaxy. Thus, more stars are sampled by a single line of sight through an edge-on than through a face-on galaxy at that same (projected) radius. Because of this, it is easier to detect light at larger radii in edge-on galaxies than in face-on galaxies. This allowed van der Kruit (1979) to note that in three edge-on galaxies, the radius of the stellar disc did not increase with deeper photographic exposures. This work was later expanded to a set of eight edge-on galaxies for which the three-dimensional light distribution was studied in detail. Each of these galaxies has a truncated disc, beyond which the intensity rapidly drops to zero, on average after 4.2 ± 0.6 radial scalelengths (van der Kruit & Searle 1981a,b, 1982a,b). The presence of truncations was confirmed by Pohlen, Dettmar & Lütticke (2000), who found however a ratio of truncation radius to exponential scalelength of only 2.9 ± 0.7.

Truncations in face-on galaxies have, at least in our view, not been unambiguously identified. Pohlen & Trujillo (2006) used the Sloan Digital Sky Survey (SDSS) to study a set of 90 face-on late-type galaxies. Pohlen & Trujillo (2006) identified 14 face-on galaxies with truncations. This result has been disputed by van der Kruit (2008), who argued that these are in fact breaks similar to those found by Freeman (1970). Erwin, Pohlen & Beckman (2008) studied 66 barred, early-type galaxies and Gutiérrez et al. (2011) another sample of 47 early-type non-barred spirals. Many of these inclined systems are classified as having 'truncations' (increasingly among later types), but we remain unconvinced that these are equivalent to those in edge-ons and not breaks at higher surface brightness levels. Combining *Spitzer* and near-IR observations seems to indicate that the break radii correlate with those of rings, lenses or spiral arms, and not with a sharp outer decline (Laine et al. 2014). Bakos, Trujillo & Pohlen (2008) found from a study of radial colour profiles that breaks in the light profiles often do not correspond to breaks in the apparent total stellar mass surface density, in fact leaving no feature whatsoever. Recently Herrmann, Hunter & Elmegreen (2013, 2016) have initiated studies of a large sample of dwarf galaxies; they find many cases of breaks that (unlike spirals) remain in stellar surface density profiles. Exponential gas discs can have a double exponential star formation rate, the break radius being related to the instability (Elmegreen & Hunter 2006). Comerón et al. (2012) studied 70 edge-on galaxies from the Spitzer Survey of Stellar Structure in Galaxies and found that many edge-ons have truncations, while often more inward breaks could be identified, that occurred at similar positions as those measured in face-on galaxies by Pohlen & Trujillo (2006).

The view of breaks and truncations as two separate features was put forward by Martín-Navarro et al. (2012). In a study of 34 highly inclined spiral galaxies, they found that the innermost break occurs at $\sim 8 \pm 1$ kpc and truncations at $\sim 14 \pm 2$ kpc in galaxies. It should be stated that not all workers agree with this point of view. In

★ E-mail: vdkruit@astro.rug.nl

particular, Erwin et al. (2008), but also Erwin, Beckman & Pohlen (2005) and Pohlen & Trujillo (2006), argue that the breaks really correspond to the truncations in edge-on galaxies. We disagree, but will return to this subject more extensively in the next paper in our studies (Peters et al. 2015).

Antitruncated profiles, in which the intensity drops less quickly beyond the break than it did before the break, have also been discovered (Erwin et al. 2005). We now further address this issue in this paper, but will discuss it in more detail in the next paper (Peters et al. 2015).

Part of the problem in detecting truncations originates in the different ways in which profiles from edge-ons and face-ons are extracted. In edge-on galaxies, the surface photometry is defined as the surface brightness along the major axis of the galaxy. This light comes from a variety of radii as the line of sight crosses through the galaxy. In face-on galaxies, the most common way to derive profiles is by performing elliptical averaging, such as that offered by the IRAF package ELLIPSE (Jedrzejewski 1987; Busko 1996). Light in such a profile only comes from structures at a single radius. The averaging cancels out any local structure, which might be causing the truncations in edge-ons (van der Kruit & Freeman 2011).

We believe that these local structures are of importance when looking for disc truncations. It is therefore interesting to see what the impact of ellipse averaging is on profiles, and to explore alternative ways to derive such profiles. We use two different methods for deriving surface brightness profiles in face-on galaxies that should be less sensitive to local structure and deviations from circular symmetry: the principal axis summation (PAS) and the equivalent profiles (EP). In Section 2, we will detail the inner workings of these methods. We will present our sample of face-on galaxies, based on a sub-sample of the work by Pohlen & Trujillo (2006), in Section 3. In Section 4, the data will be analysed and discussed, followed by the conclusions in Section 5. In order to conserve trees, the online appendix contains tables and figures for individual galaxies.

2 SURFACE PHOTOMETRY METHODS

2.1 Principal axis summation

The active debate over the nature of truncations in edge-ons versus face-ons sparked our interest in developing a new way of measuring the profiles. While attempts have been made to decompose edge-on galaxies into face-ons, such as van der Kruit & Searle (1981a), Pohlen et al. (2007), Pohlen et al. (2004), Pohlen et al. (2007) and Comerón et al. (2012), no real attempt has been made to project face-ons into edge-ons. This enticed us to develop this first method, the PAS. While not a true projection into an edge-on geometry, the PAS results resemble the edge-on geometry more closely than those using ellipse-fit profiles.

The PAS method partitions the face-on galaxy into four quadrants, centred on its major and minor axis. Each quadrant is summed on to the major axis, leaving four quadrant profiles $Q_1(R)$, $Q_2(R)$, $Q_3(R)$ and $Q_4(R)$ (see Fig. 1). These are multiplied by two, to represent the full line of sight along the major axis and to represent the line-of-sight integration in an edge-on galaxy better. The main profile $P(R)$ is taken as the median of these four. The scatter between the four quadrants is a good measure of any asymmetry in the galaxy. In cases where one or more quadrants suffer from severe contamination by foreground or background objects, that quadrant can be ignored and only the clean quadrants will be used for the median. A clear example of this is in NGC 450, where background galaxy UGC 807 is covering a significant part of a quadrant (quadrant Q2 in Fig. 1). We run a dynamic binning algorithm along the main profile, to ensure that each point has at least a signal-to-noise ratio of 2. We use an elliptical blanking mask around each galaxy, shaped and oriented according to the 25th magnitude ellipse of the galaxy and blanked beyond a trust radius R_t, to minimize the contribution of sky noise. The trust radius R_t is determined by eye on a heavily smoothed image, such that the galaxy is fully included in the mask.

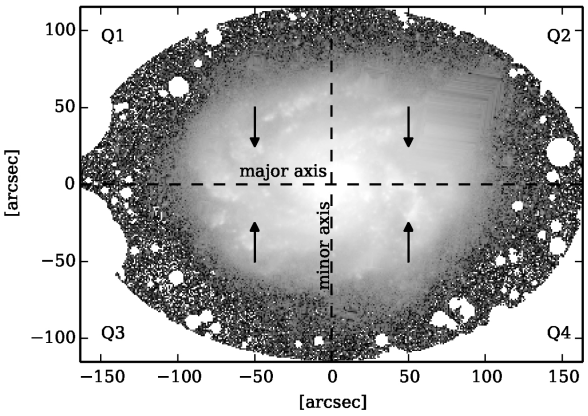

Figure 1. Demonstration of the terminology used in the PAS method. The shown galaxy is NGC 450. The major and minor axes are shown using the dashed lines. Each quadrant has been labelled. The direction in which the data are summed is shown using the arrows. The outlines of the mask covering background galaxy UGC 807 are visible in quadrant Q2. This quadrant is therefore ignored in the final PAS analysis.

The noise in each quadrants profile is a combination of the intrinsic pixel-to-pixel noise, any large-scale fluctuations and blanked regions. It thus varies with radius as the amount of pixels in the summation changes. The main profile depends on the combination of four of these varying quadrants and can thus vary drastically. To have a good representation of the noise levels, we calculate the noise in the profiles using the sky, as taken from the ellipse between one and two times the trust radius R_t. All pixels between these two radii are selected and merged row by row into a single long row of pixels. For each quadrant, we smooth a copy of this row of sky pixels with a 'tophat' kernel with the length of the amount of pixels used, effectively recreating the pixel summation. We randomly select a value out of each of these four smoothed sets and take the median. This is repeated 10 000 times and the noise is then calculated as the standard deviation of this sample.

There are two major differences between this projection and a true edge-on. First, in real edge-ons, we would be able to observe the effect of variations with height. As we are seeing the galaxy from above, PAS cannot show this effect. Compared to ellipse averaging, due to the summation the surface brightness in PAS will also be brighter. The summation effectively has the unit magnitude per arcsec, making it distance dependent. For a true comparison with edge-ons, one would therefore need to apply the PAS method to those as well. The overall shape of the profile should however be equal. A second major difference is that dust absorption is less of an issue here. In a true edge-on, this could have a significant impact on the scalelength of the profile. This is an interesting feature, as a statistical comparison in a large sample of edge-ons and face-ons could be used to analyse the dust content of galaxies.

The PAS profiles are more susceptible to sky determination issues than ellipse-fit profiles, as any remaining background offset will be multiplied by the amount of pixels along the minor axis instead

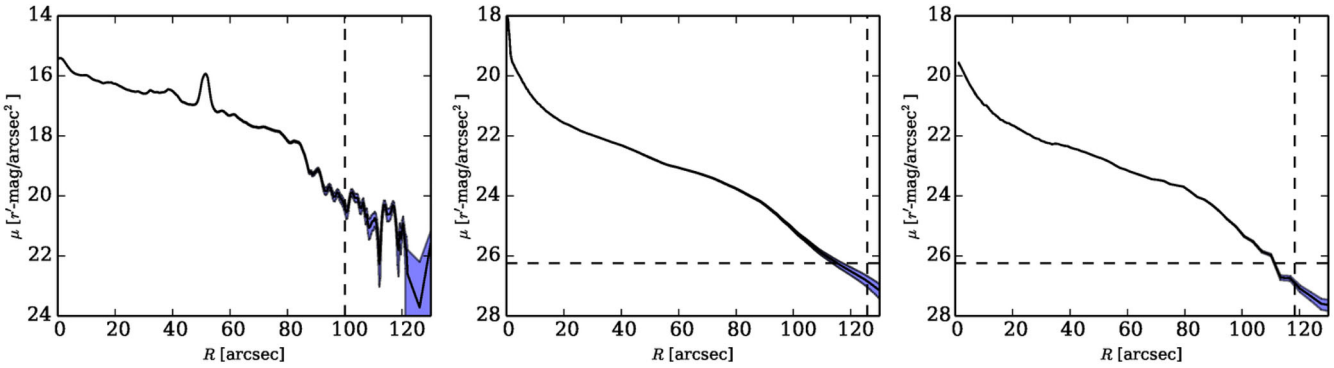

Figure 2. Demonstration of the sensitivity to background under- and overestimation. Here we have used an offset of 0.1 ADU. The horizontal dashed line shows the level of the pixel-to-pixel noise. The vertical dashed line shows the point where the profile deviates by more than 0.2 mag, which represents the point up to which we trust the profile. From left to right, the panels correspond to the PAS, EP and ellipse-fit methods. The profiles are based on NGC 450 (see Fig. A4).

of being averaged. In this paper, we will use the uncertainty in the background-offset estimation (see Section 3.6) to over- and undersubtract the profile. We place our confidence limit at the spot where these three profiles start to deviate by more than 0.2 mag. In Fig. 2 (left), the sensitivity to the background is demonstrated, by over- and undersubtracting the data by 0.1 ADU.

As noted before, the PAS profiles are effectively in units of magnitude per arcsec. Because of this, direct comparison with the other two types of profiles is hard. Still, we have chosen to display all these profiles together in one graph, by applying an offset to the PAS profiles, such that at $R = 0$ the brightest EP begins at the same magnitude as the faintest PAS profile. Direct comparisons of the brightness of the PAS profile with the EP and ellipse-fit profiles should not be made. This strategy does however allow for the check if a feature occurs at a particular radius R in all three types of profiles.

2.2 The equivalent profiles

The EP are a radical twist on the usual methods. Instead of using the radius R to find the surface brightness $\mu(R)$ in a face-on galaxy, the method turns things around. For each observed surface brightness μ in the image, there will always be some number of pixels $N(\mu)$ that have that or a brighter value. Since each pixel covers a small surface dA, a total equivalent surface $A(\mu)$ can be formed. In SDSS, the area of each pixel covers 0.396×0.396 arcsec^2. Assume that the surface brightness in a galaxy is always brightest in the centre and decreases with radius.[1] The surface will then form an ellipse, or circle in the case of a perfect face-on, centred on the galaxy. The radius of this equivalent surface is called the equivalent radius $R(\mu)$. Mathematically, we can describe this as

$$R(\mu) = \sqrt{\frac{N(\mu) dA}{\pi \cos i}}, \quad (1)$$

where i is the inclination of the galaxy.

As an example, suppose for a perfectly face-on galaxy that the brightest pixel in the observation has a value of $\mu = 18$ r' mag arcsec^{-2}. Since this value is only reached in one pixel, the equivalent area $A(\mu)$ is only 0.396^2 arcsec^2, and the equivalent radius $R(\mu)$ is thus 0.35 arcsec. At μ =20 r' mag arcsec^2, there could be 10 000 pixels at that or a brighter value. In that case, the equivalent area $A(\mu)$ goes up to $0.396^2 \times 10\,000 = 1568$ arcsec^2, and the equivalent radius $R(\mu)$ is thus 22.3 arcsec. By repeating this process for every value of μ in the observation, we can thus build up the associated set of equivalent radii.

[1] With the exception of small-scale features, this holds for all three types of profiles; the only difference between them is the rate at which the brightness decreases.

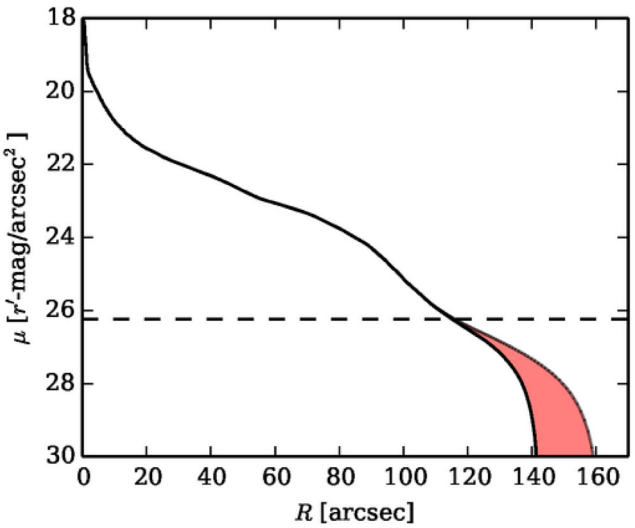

Figure 3. Effect of choice of radius for the elliptical mask on the EP. The radius of the mask has been increased by 25 per cent. The shaded region shows the increase in profile compared to the original, black profile. The horizontal dashed line shows the level of the pixel-to-pixel noise.

Tests show that this method is particularly sensitive to background noise. Any positive component of the noise distribution will add to surface $A(\mu)$ and thus increase radius $R(\mu)$. This creates a drastic increase in the equivalent radius at the faintest surface brightness levels (see for example Fig. 3). The other methods suffer much less from this, as the positive noise values are averaged out against the negative noise values. Two techniques are used to deal with this. First, similar as in the PAS, we use an elliptical blanking mask around the galaxy. It is centred on the galaxy and has sufficient radius not to blank the galaxy itself, but leaves as little background as possible. This blocks out all signals for which we are sure that they are unrelated to the galaxy. Secondly, we use non-linear anisotropic filtering, an algorithm normally used in magnetic resonance imaging (Jones, Whittall & MacKay 2003). This helps smooth low S/N

regions, while conserving the flux and important structure in the image.

EP are an old method, going back more than 60 years. The oldest reference traces back to de Vaucouleurs (1948), wherein he derives his famous $R^{1/4}$ profile. In the decades beyond, they were used quite often, as for example in the photometric survey by van der Kruit (1979). The newer elliptically averaged profiles suffer less from noise and are able to vary the position angle and inclination as a function of radius (Jedrzejewski 1987), things that the EP cannot. This is likely why the EP have fallen from grace.

Similar to the PAS, the confidence limit of the profile is again calculated by over- and undersubtracting the data by two times the uncertainty and establishing where the profiles start to deviate by more than 0.2 mag. We demonstrate this contamination by background noise in Fig. 2 (middle). Comparing it to the profiles from the elliptical averaging (reproduced here from Pohlen & Trujillo 2006), we see that the EP start to suffer at brighter magnitude levels. In practice, this level is slightly higher than the background pixel-to-pixel noise σ. The choice of the radius of the mask is also not trivial, as demonstrated in Fig. 3. The larger the radius, the more background is sampled, and the more noise is picked up. We have opted to use the same ellipse, with trust radius R_t as used for the PAS.

3 DATA

3.1 Sample

We use the full sample defined by Pohlen & Trujillo (2006). They used the following criteria to define their sample:

(i) A Hubble type T parameter between $2.99 < T < 8.49$. This corresponds to an intermediate to late-type galaxy sample with Sb to Sdm galaxies.

(ii) The axis ratio is chosen such that the inclination is $i < 61^\circ$, as to avoid the influence of dust and as a convenient way to classify the morphological properties of the galaxy that would have been more obscured at higher inclinations.

(iii) The recession velocity is $v_{\rm vir} < 3250$ km s^{-1} and the total B-band brightness $M_{\rm B,abs} < -18.5$ B mag, as to get a complete sample of galaxies within the 46 Mpc survey distance.

(iv) Galactic latitude $\|b_{II}\| > 20^\circ$ as to avoid dust obscuration.

Using DR2 of SDSS (Abazajian et al. 2004), this led them to a sample of 98 face-on galaxies for which observations were available, out of a full sample of 655 galaxies. The final sample is listed in Table 1.

3.2 Data reduction

Originally, we retrieved the SDSS images straight from the SDSS website at www.sdss.org. These came from Data Release 7 (Abazajian et al. 2009). Most of the galaxies are so large, however, that their outskirts are often not covered by the frame and mosaicking would be required. Instead of manually mosaicking these images, we opted for a different approach. We used MONTAGE[2] (Jacob et al. 2010), for the retrieval and mosaicking. In this paper, we focus on the g', r' and i' band images.

The following steps were undertaken. The reference header of the final image was created using `mHdr`. Tasks `mArchiveList`

[2] MONTAGE is available at montage.ipac.caltech.edu/.

Table 1. Fundamental properties for the full sample.

Galaxy	$M_{\rm B,abs}$	Type	t	$v_{\rm rot}$(km s^{-1})	i (°)	PA (°)	D (Mpc)
IC1067	− 18.65	Sb	3.0	148.74	42.3	151.1	28.3
IC1125	− 20.03	SBcd	7.3	103.77	55.9	305.8	35
IC1158	− 19.52	SABc	5.1	120	55.9	136.7	29.7
NGC 0450	− 19.72	SABc	5.8	102.94	50.2	188.8	19
NGC 0701	− 19.84	SBc	5.0	120.96	59.3	45.7	19.5
NGC 0853	− 16.23	Sm	8.6	60.29	50.2	16.3	21
NGC 0941	− 19.13	SABc	5.3	88.93	45.6	101.4	22
NGC 1042	− 20.27	SABc	6.0	46.1	36.9	74.7	4.21
NGC 1068	− 21.5	Sb	3.0	282.54	24.5	170.2	10.1
NGC 1084	− 20.63	Sc	4.9	194.52	52.4	52.8	16.6
NGC 1087	− 20.65	SABc	5.2	120.27	52.4	268.4	19
NGC 1299	− 19.35	SBb	3.0	120.91	56.6	42.0	32
NGC 2541	− 18.66	SABc	6.0	97.22	61.3	107.6	14.8
NGC 2543	− 20.5	Sb	3.0	148.11	60.0	51.1	26.3
NGC 2684	− 19.88	Sc	4.6	101.03	34.9	35.1	44.9
NGC 2701	− 20.45	SABc	5.2	143.88	47.2	63.3	30.7
NGC 2776	− 21.54	SABc	5.2	99.06	18.2	6.0	38.7
NGC 2967	− 20.37	Sc	5.2	165.95	21.6	250.7	30.9
NGC 3055	− 20.12	SABc	5.3	142.65	54.5	27.0	28
NGC 3246	− 19.3	Sd	7.9	109.85	58.7	354.4	35.5
NGC 3259	− 19.62	SABb	3.7	120.54	55.2	71.5	35.9
NGC 3310	− 20.11	SABb	4.0	288.38	18.2	70.7	17.5
NGC 3359	− 20.57	Sc	5.2	148.06	58.7	101.9	22.6
NGC 3423	− 19.6	Sc	6.0	127.12	35.9	56.3	11.7
NGC 3488	− 19.9	SBc	5.2	122.69	48.7	92.7	46.3
NGC 3583	− 20.58	SBb	3.1	182.1	47.2	326.4	31.6
NGC 3589	− 18.63	SABc	7.0	77.82	60.0	36.3	34.1
NGC 3631	− 21.02	Sc	5.2	78.36	32.9	339.9	21.6
NGC 3642	− 20.57	Sbc	4.0	48.71	18.2	7.4	27.5
NGC 3756	− 20.2	SABb	4.0	145.95	60.0	91.0	15.7
NGC 3888	− 20.47	SABc	5.3	203.06	42.3	335.8	41.5
NGC 3893	− 21	SABc	5.2	147.68	53.8	282.4	15.7
NGC 3982	− 19.91	SABb	3.2	191.83	27.1	92.2	24.6
NGC 3992	− 21.31	Sbc	4.0	295.12	54.5	19.8	22.9
NGC 4030	− 20.84	Sbc	4.0	201.32	36.9	59.6	25
NGC 4041	− 20.19	Sbc	4.0	263.1	18.2	12.4	22.7
NGC 4102	− 19.4	SABb	3.1	158.14	55.2	50.6	16
NGC 4108	− 20.25	Sc	5.2	223.28	39.6	323.1	41.6
NGC 4108B	− 18.77	SABc	7.0	195.8	38.7	349.7	43.8
NGC 4123	− 19.91	Sc	5.0	128.5	47.9	324.0	14.9
NGC 4210	− 19.99	Sb	3.0	162.96	40.5	351.9	44.8
NGC 4273	− 20.6	Sc	5.2	328.91	52.4	263.3	28.5
NGC 4480	− 20.3	SABc	5.1	169.24	60.0	92.6	36.7
NGC 4517A	− 19.8	Sd	7.8	71.35	55.2	241.4	23.6
NGC 4545	− 20.3	Sc	5.6	129.19	54.5	264.7	38.2
NGC 4653	− 20.33	SABc	6.0	211.75	33.9	101.5	39.1
NGC 4668	− 18.92	SBcd	7.4	62.33	58.7	265.5	17.2
NGC 4904	− 19.12	Sc	5.8	105.15	44.8	243.4	20.5
NGC 5147	− 19.09	SBd	7.9	154.83	37.8	150.5	21.6
NGC 5300	− 18.7	SABc	5.2	120.42	47.9	119.6	19.9
NGC 5334	− 19.12	Sc	5.2	132.75	39.6	76.0	24.7
NGC 5376	− 20.03	SABa	2.3	204.71	52.4	208.9	55.5
NGC 5430	− 20.76	SBb	3.1	186.86	49.5	87.4	37.9
NGC 5480	− 19.94	Sc	5.0	150.36	31.8	231.8	22.4
NGC 5584	− 19.69	SABc	6.0	124.86	42.3	292.1	19.7
NGC 5624	− 18.75	Sbc	3.8	66.52	48.7	71.8	35
NGC 5660	− 20.66	SABc	5.2	138.52	18.2	129.6	37.2
NGC 5667	− 19.93	SBc	6.0	100.4	58.0	100.1	34.8
NGC 5668	− 20.01	Scd	6.9	72.52	31.8	134.0	26.9
NGC 5693	− 19.08	Scd	6.9	44.83	18.2	139.6	40.1
NGC 5713	− 21.16	SABb	4.0	107.91	29.5	81.6	18.3
NGC 5768	− 19.43	Sc	5.3	123.62	27.1	337.4	33.1
NGC 5774	− 19.37	SABc	6,9	83.64	38.7	135.1	26.8
NGC 5806	− 19.92	Sb	3,2	190.93	57.3	104.7	25.2

Table 1 – *continued*

Galaxy	$M_{B,abs}$	Type	t	v_{rot}(km s^{-1})	i (°)	PA (°)	D (Mpc)
NGC 5850	– 21.5	Sb	3,1	117.44	38.7	103.4	28.5
NGC 5937	– 21.17	SABb	3,2	180.29	55.9	70.9	46.6
NGC 6070	– 21.14	Sc	6,0	204.85	64.5	210.8	27.8
NGC 6155	– 20.02	Sc	5,2	109.64	43.9	133.3	41.7
NGC 7437	– 18.75	SABc	6,7	151.78	25.8	70.9	29.2
NGC 7606	– 21.2	Sb	3,0	445.74	67.7	125.7	31
PGC006667	– 18.28	Scd	6,6	136.08	35.9	328.0	24.6
UGC02081	– 18.39	SABc	5,8	95.56	54.5	108.8	42.5
UGC04393	– 19.23	Sbc	3,5	62.21	56.6	29.0	15.2
UGC06309	– 19.74	SBc	4,5	134.19	46.4	326.5	47
UGC06518	– 19.06	Sbc	3,8	87.56	52.4	68.7	46.3
UGC06903	– 18.35	Sc	5,9	163.69	28.4	131.9	30.5
UGC07700	– 18.87	Sd	7,9	84.98	40.5	200.7	48.3
UGC08041	– 18.48	SBcd	6,9	103.6	58.7	290.0	17.2
UGC08084	– 18.84	SBd	8,0	88.77	34.9	210.5	41.1
UGC08237	– 19.82	SBb	3,0		38.7	138.5	47
UGC08658	– 19.93	Sc	5,0	124.79	52.4	160.3	37.2
UGC09741	– 18.84	Sbc	4,0		27.1	102.3	42.9
UGC09837	– 19.48	SABc	5,3	179.15	18.2	117.6	41.2
UGC10721	– 19.72	Sc	5,8	143.07	47.9	159.8	45.8
UGC12709	– 19.05	SABm	8,7	70.61	52.4	13.0	35.1

and `mArchiveExec` were then used in sequence to retrieve the g', r' and i' images from SDSS. The images were then projected to the reference frame using `mProjExec`. The overlap regions between the images were calculated and extracted, using `mOverlaps` and `mDiffExec`. With `mFitExec`, the plane-fitting coefficients were calculated between all frames. A model of the background was then created using `mBgModel`. We did allow it to fit the slope and set the maximum number of iterations to 5. We corrected all frames to the common background using `mBgExec`. Finally, the images were joined using `mAdd`.

Each galaxy is thus composed of a set of SDSS frames, which all have a background plane subtracted. We have also run a test wherein only a constant offset correction was performed between frames, but in almost all cases, the plane-corrected images were superior to the constant-offset-corrected images. Only in the case of some large galaxies, such as NGC 1042 and NGC 1068, did this approach fail and we were forced to remove these galaxies from our sample.

The mosaicking of images depends heavily on the correctness of the attached world coordinate system in each frame. The supplied coordinates were correct for all images, except for NGC 4210, where we found that stars were duplicated at multiple positions in the final mosaics. We corrected this using the `solve-field` tool from the astrometry.net project to verify and correct all headers automatically (Lang et al. 2010). This was done directly after downloading the raw SDSS images using `mArchiveExec`.

3.3 Calibration

Having created mosaics for the g', r' and i' bands, we need to calibrate them to mag arcsec^{-2}. Similar to Pohlen et al. (2004), we use the TsField table files associated with the original observation to get the photometric zero-point *aa*, the extinction term *kk* and the *airmass* coefficients. The surface brightness zero-point is calculated as

$$\mu_0 = -2.5 \times (0.4 \times [aa + kk \times \text{airmass}]) \quad (2)$$

$$+ 2.5 \times \log_{10}(53.907\,456 \times 0.396^2), \quad (3)$$

with an exposure time of 53.907 456 s and an area per pixel of 0.396^2 arcsec^2. The final surface brightness is then calculated as

$$\mu = -2.5 \log_{10}(\text{counts}) + \mu_0. \quad (4)$$

A series of reference stars was then selected in both the calibrated image and the mosaic. For both images, we measure the magnitudes of these stars. Using a linear fit to these magnitudes, the mosaic was then adjusted to match the calibration. On average, around 15 stars were used, with a matching error below 0.05 mag.

As we noted before in Section 2, the PAS method has units of mag arcsec^{-1} rather than mag arcsec^{-2}, effectively making the value dependent on the projected size of the minor axis of the galaxy. We still follow the above calibration strategy for the PAS, but in all subsequent plots will add or subtract a linear constant term such that the least bright PAS profile (typically the i') starts at the same value as the brightest EP (typically the g'). This is purely meant to guide the eye in direct comparisons between the various profiles and should not be seen as the true calibration.

3.4 Centring

Michael Pohlen kindly provided us with the tables from Pohlen & Trujillo (2006). We used the values therein to estimate the centre and position angle of the images, based on the 25th magnitude ellipse. The images were rotated to have their major axis aligned with the horizontal axis of the image. Overall, this scheme worked well, and only in some cases did we have to tweak the position angle manually to better correspond to the image.

3.5 Masking

Foreground stars and background galaxies are a strong contaminant of the surface brightness profiles. SEXTRACTOR was used to create an initial set of masks, based on the r'-band data set. For masks outside the galaxy, set by the outer radius of the ellipse-fit profiles, we set the masked regions to zero. Doing that inside the galaxy would create holes in the profile, so a way to average over these parts was required. We therefore use the IRAF package `fixpix` to interpolate the good parts of the image into the masked region. While far from perfect, this is the best solution for inner regions. If an object has not been fully masked, its unmasked pixels will contaminate the interpolation. An RGB (red–green–blue) image was therefore created from the three bands, and the quality of the masks was inspected. We tweak the mask by hand and recreate the RGB image. This process is repeated until we are satisfied with the result. In some cases, the contamination is too strong. We then resort to disabling those quadrants in the minor-axis integrated profiles. The EP lack such a feature, and in some cases, they clearly suffer for it. For the worst cases, we therefore remove these galaxies from our sample.

As an alternative scheme for future work, it would also have been possible to replace the values of the masking with the expected values as measured through an initial ellipse fit. However, the advantage of using our `fixpix` solution is that we make use of the local structure of the galaxy, rather than introduce an idealized symmetric version of the galaxy.

3.6 Background subtraction

Background subtraction is a famous problem in SDSS images, where due to the storage of numbers as integers one can only measure the background using very large samples (Pohlen & Trujillo

2006). We perform a run of ELLIPSE on the data using the default parameters but with fixed inclination, centre and position angle. The background offset is taken as the mean value of all results between one and two times the $R_{\rm outer}$. Here we use $R_{\rm outer}$ to denote the outermost projected radius of our profile extraction region, which will cover a region well beyond the galaxy. The 1σ background noise σ is taken by measuring the standard deviation of all pixels in that same region. The uncertainty estimation is performed by using the PYTHON `scipy.stats.bayes_mvs` to perform a Bayesian fit of a normal distribution to the background. The uncertainty is based on the average confidence limit for the mean.

In the online appendix, we present RGB images of the background, based on the three bands for selected galaxies. In regions of the image where an overlap occurs between two SDSS frames, there is a better signal-to-noise ratio due to the double observing time spent at those positions. Since the position of the individual frames that make up an image are not identically placed, this leads to locally different colours in the RGB images. This is expected and we therefore do not worry about this. However, it does imply that the background does not have a constant noise level throughout the entire image. While this is not in itself a bad thing, it is worth keeping in mind when examining the profiles with regard to the uncertainty limit. The mosaicking also introduces (low) correlated noise by regridding (averaging) the pixels. After that, all images are inspected for the flatness of the background; we are left with a sample of 57 galaxies with a stable background.

4 RESULTS

4.1 Classifications

We classify the profiles by eye for each method. While there will always be some observer bias in the classification, we try to minimize this by only distinguishing into three main classes of profiles. We follow the basic classification scheme proposed by Erwin et al. (2008). The first class, type I, is used to classify galaxies that exhibit a more or less constant exponential decay, as known from the work by Patterson (1940), de Vaucouleurs (1948) and Freeman (1970). The type II profiles will denote all galaxies that show a downward break/bend in their profile, similar to Freeman (1970). The type III profiles refer to the so-called 'anti-truncated' profiles, as first reported by Erwin et al. (2005). In these profiles, there is a steep descent of the light, followed by a less steep descent. Unlike Pohlen & Trujillo (2006) and Erwin et al. (2008), we do not sub-classify these profiles further.

There are no fixed criteria to quantify at which point a profile shows so many features that it stops being a simple type I profile, and we tend to classify more galaxies as type II compared to Pohlen & Trujillo (2006). Four galaxies are classified as type I, 40 galaxies are of type II and 16 are of type III. Note that some galaxies are associated with multiple classifications simultaneously. Overall, the profile classification is the same, independent of the type of profile. Including the mixed types in each category, the ratios are 7 per cent of the galaxies as type I, 70 per cent as type II and/or 28 per cent as type III. Comparing this with the original classifications by Pohlen & Trujillo (2006), their classifications would have been 12 per cent in type I, 65 per cent in type II and 35 per cent in type III. Twenty-nine galaxies in this sample are classified by us as purely type II galaxies, of which four have been classified by Pohlen & Trujillo (2006) as type I and five have been classified by them as both types II and III. In total, we match the complete classification by Pohlen & Trujillo (2006) for 40 out of 57 galaxies (70 per cent).

The type III galaxies are an interesting set. Most of these galaxies show clear signs of interaction, be it an asymmetric disc (e.g. NGC 853, Fig. A6) or tidal tails (e.g. NGC 3631, Fig. A22; NGC 3642, Fig. A23). This has already been reported by van der Kruit & Freeman (2011), who noted that many of the type III galaxies are mergers. Table 2 shows all classifications.

4.2 Measurement of scalelengths and feature radii

Measurement of the scalelengths was done in the following way. For each galaxy, we have seven profiles (r' ellipse, and g', r' and i' for both EP and PAS). We select the most prominent feature in the profile by eye and try to define a fit region on either side of the feature, where the profiles are showing more or less linear behaviour. For the region before the feature, its outer radii are denoted by R_1 and R_2, while after the feature the radii are R_3 and R_4. Table 2 in the online appendix shows all these radii.

Knapen & van der Kruit (1991) showed that the choice of radii to which a profile is fitted, has a strong effect on the derived scalelengths. To avoid the introduction of a bias, we use the same region for all of our profiles. This can result in a different position for the feature per technique, and in some cases we find that the fitting favours different features entirely. We therefore classify the overall goodness of fit for the entire fitting result by eye. We only focus our statistical analysis on the galaxies having goodness-of-fit quality flag 'G' and a purely type II profile. This limits our statistics sample to 29 galaxies. The scalelengths are listed in Table 3.

We denote the scalelengths measured before the feature as the inner scalelength h_0 and after the feature as outer scalelength $h_{\rm f}$. The feature radius is denoted by $R_{\rm f}$, where any additional subscript will be used to refer to the specific method used. The feature surface brightness μ is measured as the surface brightness of the profile at the feature radius $R_{\rm f}$. The radii and surface brightness are listed per galaxy in Table 4. The colours are listed in Table 5.

The following method is used to estimate the errors. From each fit region, we randomly drop 10 per cent of the points. A linear fit is performed to the remaining 90 per cent. In cases where multiple fit regions are defined, we perform this simultaneously in every region. The resulting fits will be slightly different compared to the original fits. By proxy, the resulting feature radii and feature surface brightness will also be different. By repeating this process 100 times, a scatter distribution builds up for each variable. We measure the standard deviation from each distribution, and define the error as half-width half-maximum by multiplying it by $\sqrt{2\ln 2}$. In some cases, we find that not all fits return a realistic result. This occurs particularly in the more noisy regions. When this occurs, the error bars are denoted using arrows in all subsequent graphics.

4.3 Sub-classification into breaks and truncations

After studying a sample of edge-on galaxies, Martín-Navarro et al. (2012) proposed to distinguish between breaks and truncations based on the criterion $R_{\rm f}/h_{\rm f} = 5$. All values above 5 were considered truncations, while all values lower were considered breaks. We show the histogram of $R_{\rm f}/h_{\rm f}$ for our sample in Fig. 4. Twelve truncations are found in the PAS sample. Seven galaxies in the EP can be considered truncations, out of which six overlap with the PAS sample. We list the truncation sample in Table 6, along with pointers to the figures of the individual galaxies in the online appendix. For clarity, we repeat that we only include here the galaxies having goodness-of-fit quality flag 'G' and a purely type II profile.

Table 2. Quality and fit radii for the approved image sample. Profile quality is split into types bad, moderate and good. Radii in arcsec.

Galaxy	Quality		Type	Fit radii			
	Image	Profile		r_1	r_2	r_3	r_4
IC1067	G	M	I	30	80		
IC1125	G	G	II	30	40	45	60
IC1158	G	G	II	40	60	70	100
NGC 0450	G	G	II	40	75	84	100
NGC 0701	G	B	I in ellipse, II in PAS	20	60	60	80
NGC 0853	G	B	III in EP and Ell, I in PAS	25	50	50	70
NGC 0941	G	G	II	20	65	70	110
NGC 1299	G	M	II in PAS, III in EP and ellipse	0	25	30	70
NGC 2701	G	G	II and III	20	40	50	70
NGC 2776	G	B	II in PAS, III in EP and ellipse	20	80	80	140
NGC 2967	G	G	III	20	50	90	140
NGC 3055	G	G	II	20	55	60	80
NGC 3259	G	G	III	20	40	50	100
NGC 3423	G	G	II	30	85	100	140
NGC 3488	G	M	II and III	20	30	40	60
NGC 3589	G	G	II	10	28	35	50
NGC 3631	G	M	II (EP fails due to variations)	55	100	120	170
NGC 3642	G	M	III	15	75	80	150
NGC 3888	G	M	II	20	45	45	70
NGC 3982	G	G	III	20	40	50	80
NGC 4041	G	G	III	40	70	85	150
NGC 4102	G	G	II	20	60	60	90
NGC 4108	G	B	II	10	40	50	60
NGC 4108B	G	B	I in ellipse, II in PAS	0	40	40	55
NGC 4273	G	B	II	40	60	80	120
NGC 4545	G	G	II	20	60	60	70
NGC 4653	G	G	II	20	80	105	125
NGC 4668	G	M	II and III	20	33	40	50
NGC 4904	G	G	II	15	35	50	80
NGC 5147	G	G	II	7	35	40	70
NGC 5300	G	G	II	13	75	100	140
NGC 5334	G	G	II	40	80	100	140
NGC 5376	G	G	II	10	30	40	70
NGC 5430	G	G	II	30	48	60	90
NGC 5480	G	G	III	20	40	80	120
NGC 5624	G	B	III in EP and Ell, I in PAS	20	40	40	80
NGC 5660	G	M	II	20	60	70	80
NGC 5667	G	B	II (EP fails due to variations)	10	35	45	60
NGC 5668	G	G	II	50	80	85	100
NGC 5693	G	G	II	10	30	40	70
NGC 5713	G	B	I in ellipse, I in PAS	50	85	100	130
NGC 5774	G	G	II	20	80	85	130
NGC 5806	G	M	III	50	100	150	200
NGC 6155	G	M	II	0	30	40	60
NGC 7437	G	G	II	20	40	50	80
PGC006667	G	G	II	30	70	80	110
UGC02081	G	G	II	0	55	60	90
UGC04393	G	B	II	40	60	60	70
UGC06309	G	B	II	20	40	40	60
UGC06518	G	G	II	10	25	25	38
UGC06903	G	G	II	20	50	60	95
UGC07700	G	G	II	20	39	49	80
UGC08084	G	G	II	11	40	45	60
UGC08658	G	G	II	20	49	55	90
UGC09741	G	G	III	10	20	25	40
UGC09837	G	G	II	20	45	53	67
UGC12709	G	G	II	31	75	75	100

Overall, we see that most of the EP R_f/h_f values lie in a compact range from 1.5 to 6. The PAS values span a wider range, between 1.0 and 10, and are more evenly spread. In the edge-on sample from Martín-Navarro et al. (2012), the R_f/h_f ranges from 1 to 20. The mean values of R_f/h_f for the ellipse-fit profiles are 4.46 ± 2.86, for the EP 4.02 ± 1.67 and for the PAS 4.71 ± 5.14. The wider spread of the PAS appears to represent edge-on profiles better than the EP. It is interesting to note that the EP have a lower average value and

Table 3. Derived scalelengths for the ellipse-fit and EP. Units in kpc. Errors are formal. The slopes of the PAS profiles are los-convolved and therefore not directly translatable into scalelengths, so we have omitted results from that method.

	Ellipse		Equivalent profiles					
Galaxy	h_0 r'	h_f r'	h_0 r'	h_f r'	h_0 g'	h_f g'	h_0 i'	h_f i'
IC1125	2.64 ± 0.05	1.63 ± 0.06	2.48 ± <0.01	1.66 ± <0.01	2.72 ± <0.01	1.69 ± <0.01	2.38 ± <0.01	1.95 ± <0.01
IC1158	3.53 ± 0.10	1.49 ± 0.03	3.23 ± <0.01	1.51 ± <0.01	3.22 ± <0.01	1.66 ± <0.01	3.34 ± <0.01	1.69 ± <0.01
NGC 0450	2.74 ± 0.03	1.32 ± 0.07	3.00 ± <0.01	1.35 ± <0.01	3.07 ± <0.01	1.35 ± <0.01	2.92 ± <0.01	1.42 ± <0.01
NGC 0941	2.11 ± 0.01	1.48 ± 0.04	2.15 ± <0.01	1.71 ± <0.01	2.20 ± <0.01	1.71 ± <0.01	2.17 ± <0.01	1.95 ± <0.01
NGC 2701	3.71 ± 0.04	1.20 ± 0.01	3.53 ± <0.01	1.22 ± <0.01	3.79 ± <0.01	1.20 ± <0.01	3.44 ± <0.01	1.40 ± <0.01
NGC 2967	2.48 ± 0.01	5.50 ± 0.13	2.50 ± <0.01	5.56 ± 0.01	2.56 ± <0.01	5.77 ± 0.02	2.49 ± <0.01	5.95 ± 0.01
NGC 3055	2.43 ± 0.02	1.30 ± 0.02	2.20 ± <0.01	1.18 ± <0.01	2.22 ± <0.01	1.17 ± <0.01	2.24 ± <0.01	1.22 ± <0.01
NGC 3259	2.06 ± 0.01	4.83 ± 0.09	2.07 ± <0.01	4.81 ± 0.01	2.27 ± <0.01	4.86 ± <0.01	2.07 ± <0.01	5.10 ± 0.01
NGC 3423	2.81 ± 0.03	0.95 ± 0.01	2.39 ± <0.01	1.01 ± <0.01	2.51 ± <0.01	1.02 ± <0.01	2.35 ± <0.01	1.04 ± <0.01
NGC 3589	3.39 ± 0.04	1.59 ± 0.02	3.06 ± <0.01	1.49 ± <0.01	3.31 ± <0.01	1.39 ± <0.01	3.13 ± <0.01	1.64 ± <0.01
NGC 3982	1.23 ± 0.01	1.90 ± 0.04	1.26 ± <0.01	1.94 ± <0.01	1.27 ± <0.01	2.08 ± <0.01	1.28 ± <0.01	1.90 ± <0.01
NGC 4041	1.94 ± 0.01	3.22 ± 0.05	2.03 ± <0.01	3.93 ± 0.01	1.98 ± <0.01	4.05 ± 0.01	2.12 ± <0.01	4.49 ± 0.01
NGC 4102	2.76 ± 0.06	1.19 ± <0.01	2.46 ± <0.01	1.14 ± <0.01	2.36 ± <0.01	1.15 ± <0.01	2.52 ± <0.01	1.16 ± <0.01
NGC 4545	3.11 ± 0.01	2.21 ± 0.10	3.10 ± <0.01	2.16 ± <0.01	3.22 ± <0.01	2.00 ± <0.01	3.12 ± <0.01	2.25 ± <0.01
NGC 4653	4.34 ± 0.02	2.74 ± 0.14	4.39 ± <0.01	3.30 ± <0.01	4.67 ± <0.01	3.10 ± 0.01	4.34 ± <0.01	3.31 ± 0.01
NGC 4904	2.77 ± 0.02	1.26 ± 0.01	2.19 ± <0.01	1.20 ± <0.01	2.42 ± <0.01	1.15 ± <0.01	2.09 ± <0.01	1.25 ± <0.01
NGC 5147	2.34 ± 0.03	1.22 ± 0.01	2.01 ± <0.01	1.22 ± <0.01	2.20 ± <0.01	1.18 ± <0.01	1.93 ± <0.01	1.25 ± <0.01
NGC 5300	3.64 ± 0.01	1.68 ± 0.02	3.50 ± <0.01	1.87 ± <0.01	3.83 ± <0.01	1.82 ± 0.01	3.43 ± <0.01	1.94 ± <0.01
NGC 5334	4.67 ± 0.03	2.21 ± 0.11	4.78 ± <0.01	2.34 ± <0.01	5.00 ± <0.01	2.40 ± <0.01	4.69 ± <0.01	2.57 ± <0.01
NGC 5376	4.92 ± 0.04	3.05 ± 0.01	4.76 ± <0.01	3.11 ± <0.01	4.97 ± 0.01	3.09 ± <0.01	4.67 ± <0.01	3.22 ± <0.01
NGC 5430	4.23 ± 0.06	2.14 ± 0.04	3.40 ± <0.01	2.31 ± <0.01	3.50 ± <0.01	2.37 ± <0.01	3.37 ± <0.01	2.43 ± <0.01
NGC 5480	1.33 ± 0.01	2.91 ± 0.14	1.22 ± <0.01	1.91 ± 0.02	1.14 ± <0.01	1.83 ± 0.02	1.30 ± <0.01	1.65 ± 0.03
NGC 5668	4.99 ± 0.11	3.20 ± 0.02	4.20 ± <0.01	3.35 ± <0.01	4.18 ± <0.01	3.09 ± <0.01	4.17 ± <0.01	3.71 ± <0.01
NGC 5693	3.30 ± 0.03	1.78 ± 0.05	2.92 ± <0.01	2.02 ± <0.01	3.22 ± <0.01	1.89 ± <0.01	2.81 ± <0.01	2.10 ± <0.01
NGC 5774	4.25 ± 0.06	3.08 ± 0.05	4.40 ± <0.01	3.18 ± 0.01	4.47 ± 0.01	3.01 ± 0.01	4.34 ± <0.01	3.39 ± <0.01
NGC 7437	3.59 ± 0.03	2.18 ± 0.02	3.44 ± <0.01	2.25 ± <0.01	3.36 ± <0.01	2.15 ± <0.01	3.51 ± <0.01	2.36 ± <0.01
PGC006667	2.94 ± 0.03	1.48 ± 0.07	2.80 ± <0.01	1.75 ± 0.01	2.77 ± <0.01	1.40 ± 0.01	2.94 ± <0.01	2.04 ± 0.01
UGC02081	3.43 ± 0.03	1.73 ± 0.15	3.87 ± <0.01	2.92 ± 0.01	3.98 ± <0.01	2.91 ± 0.02	3.75 ± <0.01	3.06 ± 0.02
UGC06518	1.53 ± 0.01	1.36 ± 0.04	1.53 ± <0.01	1.38 ± <0.01	1.54 ± <0.01	1.31 ± <0.01	1.55 ± <0.01	1.45 ± <0.01
UGC06903	5.13 ± 0.09	1.50 ± 0.04	5.46 ± <0.01	1.80 ± <0.01	6.04 ± <0.01	1.68 ± <0.01	5.11 ± <0.01	1.97 ± <0.01
UGC07700	9.83 ± 0.17	2.18 ± 0.12	5.68 ± <0.01	2.92 ± 0.01	5.54 ± <0.01	2.74 ± <0.01	6.16 ± <0.01	3.43 ± <0.01
UGC08084	5.92 ± 0.11	1.63 ± 0.09	4.28 ± <0.01	2.09 ± 0.01	4.22 ± <0.01	1.98 ± <0.01	4.44 ± 0.01	2.40 ± <0.01
UGC08658	4.10 ± 0.03	2.92 ± 0.03	4.07 ± <0.01	3.17 ± <0.01	4.44 ± <0.01	3.24 ± <0.01	3.92 ± <0.01	3.35 ± <0.01
UGC09741	1.02 ± 0.01	2.55 ± 0.03	1.12 ± <0.01	2.48 ± <0.01	0.99 ± <0.01	2.55 ± <0.01	1.21 ± <0.01	2.48 ± <0.01
UGC09837	3.89 ± 0.08	1.39 ± 0.05	3.51 ± <0.01	1.67 ± 0.01	3.69 ± <0.01	1.52 ± <0.01	3.47 ± <0.01	1.99 ± 0.01
UGC12709	5.48 ± 0.09	2.15 ± 0.09	4.98 ± 0.01	2.61 ± <0.01	4.97 ± 0.01	2.16 ± <0.01	4.98 ± <0.01	2.88 ± 0.01

scatter than the ellipse-fit profiles. This is due to the redistribution of light that occurs as part of the EP method, which has the effect of smoothing out the profile a bit. In Fig. 5, we show boxplots for all three distributions of R_f/h_f. As can be seen more clearly from this figure, the median values of the R_f/h_f distributions are similar between the three distributions. We perform an ANOVA test on the three distributions of R_f/h_f, using *R*, to test if the difference in variance is statistically significant. We find an *F*-value of 1.356, which is not statistically significant.

4.4 Correlation tests

Following Pohlen & Trujillo (2006), we perform a range of correlation tests on all our parameters. We use the Spearman rank correlation coefficient[3] ρ to estimate if there is any monotone correlation between two parameters. We also calculate the corresponding significance p of that ρ, using as a null hypothesis the absence of correlation. We reject the null hypothesis when $p < 0.05$. The significance test p only describes the chance of finding a particular value of ρ less than or equal to the observed value purely by chance. Because of small-number statistics, very strong correlations need few samples to become statistically significant. Fainter, but potentially real, correlations require far more samples to distinguish from random noise. As our sample is small, we can only report on relatively strong correlations.

In all subsequent figures, we print the correlation of the combined feature set. The symbols distinguish between breaks and truncations using filled and open markers. The full subset correlation tests can be found in Table 7 in the online appendix. We will discuss the various correlations in the following subsections. Only the most prominent correlations are shown in figures.

4.4.1 *Scalelengths and radii*

The r'-band inner and outer scalelengths are shown in Figs 6 and 7. From Fig. 6, we find that inner scalelengths, as measured in both the EP and PAS profiles compared to the ellipse-fit profile, follow very tight positive correlations. This holds for both the full sample and the sub-samples of truncations and breaks. The PAS profiles have slightly more scatter, and thus the correlations are weaker than those of the EP with the ellipse-fit method. A line is fit through the

[3] We calculate the Spearman rank correlation coefficient ρ and significance p using the PYTHON package `scipy.stats.spearmanr`.

Table 4. Derived break radii. Radii are given in arcsec.

	Ellipse		EP						PAS					
Galaxy	R_f r'		R_f r'		R_f g'		R_f i'		R_f r'		R_f g'		R_f i'	
IC1125	6.978	0.166	6.910	<0.001	6.656	0.003	6.147	0.003	7.050	0.066	7.095	0.027	7.484	0.067
IC1158	11.575	0.103	11.801	0.006	11.522	0.002	11.849	0.005	11.551	0.041	11.318	0.067	11.687	0.056
NGC 0450	14.471	0.137	14.077	0.003	13.962	0.002	14.121	0.002	13.535	0.106	13.792	0.041	13.071	0.120
NGC 0941	13.509	0.157	13.087	0.013	12.749	0.011	14.655	0.014	12.039	0.078	12.126	0.076	11.469	0.145
NGC 2701	7.322	0.035	7.386	0.004	7.377	0.004	7.159	0.004	6.851	0.062	6.943	0.033	6.800	0.045
NGC 2967	14.364	0.118	14.128	0.004	14.075	0.010	13.881	0.007	14.927	0.092	14.088	0.092	14.149	0.070
NGC 3055	9.046	0.082	9.638	<0.001	9.470	0.002	9.690	0.001	9.548	0.087	9.801	0.067	9.015	0.070
NGC 3259	8.762	0.067	8.344	0.003	8.661	0.002	8.264	0.004	7.532	0.105	8.531	0.126	7.844	0.095
NGC 3423	15.077	0.115	15.462	0.002	15.154	0.008	15.563	0.001	16.490	0.053	15.880	0.043	16.595	0.046
NGC 3589	6.039	0.053	5.894	0.001	5.850	0.001	5.904	<0.001	5.307	0.023	5.283	0.030	4.825	0.059
NGC 3982	9.260	0.077	9.200	0.006	9.091	0.001	9.271	0.004	7.179	0.074	7.327	0.056	7.673	0.091
NGC 4041	13.233	0.134	14.211	0.009	14.570	0.006	14.190	0.008	14.644	0.253	15.977	0.334	13.289	0.307
NGC 4102	9.317	0.059	10.232	<0.001	10.378	0.002	10.165	<0.001	9.550	0.058	9.549	0.059	9.534	0.049
NGC 4545	9.708	0.174	9.991	0.001	10.086	0.001	10.130	0.001	9.651	0.037	9.583	0.032	9.920	0.023
NGC 4653	19.023	0.138	15.169	0.005	15.479	0.022	16.104	0.027	16.377	0.220	16.472	0.035	17.143	0.051
NGC 4904	7.271	0.043	8.358	0.005	7.938	0.004	8.731	0.011	7.369	0.024	7.106	0.028	7.152	0.032
NGC 5147	4.909	0.062	5.098	0.001	5.240	<0.001	5.191	0.002	5.643	0.035	5.975	0.038	5.875	0.050
NGC 5300	13.997	0.111	13.205	0.027	12.824	0.042	13.463	0.020	15.143	0.066	14.825	0.087	14.957	0.074
NGC 5334	16.679	0.259	16.117	0.008	15.778	0.006	16.165	0.006	14.847	0.094	14.308	0.061	15.967	0.052
NGC 5376	5.054	0.054	4.989	0.001	4.882	0.003	5.010	0.001	5.938	0.032	5.568	0.039	5.947	0.031
NGC 5430	8.756	0.164	9.778	0.002	9.212	0.012	9.843	0.006	8.795	0.027	8.360	0.050	8.643	0.041
NGC 5480	10.239	0.213	5.556	0.175	5.061	0.221	−0.523	1.000	4.314	0.146	5.497	0.174	6.705	0.185
NGC 5668	11.563	0.088	12.335	0.002	12.645	0.003	9.263	0.021	14.602	0.057	13.225	0.112	14.102	0.066
NGC 5693	6.329	0.157	6.527	0.004	6.224	0.003	6.680	0.002	6.085	0.048	6.488	0.065	5.890	0.102
NGC 5774	16.470	0.416	16.426	0.005	15.913	0.034	17.501	0.008	13.589	0.057	14.263	0.066	14.282	0.069
NGC 7437	6.316	0.095	5.973	0.004	5.704	0.013	6.302	0.007	7.311	0.059	7.080	0.119	4.729	0.249
PGC006667	12.400	0.259	11.955	0.036	12.541	0.036	12.246	0.058	12.875	0.112	12.808	0.102	12.854	0.228
UGC02081	12.189	0.194	10.943	0.008	10.003	0.037	10.532	0.038	9.891	0.131	8.947	0.193	9.354	0.148
UGC06518	4.439	0.985	4.806	0.017	4.468	0.001	4.960	0.027	4.198	0.065	4.211	0.022	4.124	0.070
UGC06903	10.587	0.085	9.965	0.004	9.991	0.002	9.835	0.005	9.816	0.049	10.070	0.060	9.429	0.051
UGC07700	7.569	0.143	7.398	0.010	7.836	0.005	6.607	0.004	8.284	0.072	8.786	0.072	7.471	0.194
UGC08084	6.887	0.121	6.762	0.009	6.840	0.004	6.754	0.006	6.868	0.070	5.449	0.095	5.664	0.312
UGC08658	10.209	0.101	9.605	0.002	9.695	0.003	9.269	0.011	8.928	0.106	9.090	0.092	10.540	0.089
UGC09741	3.647	0.030	3.681	0.001	3.667	0.001	3.774	0.001	3.433	0.035	3.008	0.039	3.212	0.063
UGC09837	8.569	0.070	8.032	0.011	8.182	0.005	7.824	0.014	8.532	0.046	8.747	0.046	8.978	0.091
UGC12709	12.401	0.136	12.104	0.007	11.980	0.005	12.313	0.020	13.096	0.037	12.311	0.136	12.808	0.087

data, using absolute differences as the cost function, and forcing the line through (0, 0). We find that $h_{0,\,\mathrm{EP}} \sim 0.95\,h_{0,\mathrm{ell}}$ and $h_{0,\,\mathrm{PAS}} \sim 1.11\,h_{0,\mathrm{ell}}$. The first relation is likely a result of the inability of the EP method to deal with bumps that the ellipse fit can show. If a bump is present in the ellipse-fit profile, this can make the scalelength in the ellipse-fit profile slightly steeper than that of the EP, at least at larger radii than the bump.

Another point to note is more profound: inner scalelengths of the PAS are longer than the profiles in ellipse-fit profiles. Likely this result is due to the geometry of the galaxies. The consequence is that in an edge-on galaxy without dust, the inner scalelengths will be longer. The mean inner scalelength h_0 was 3.16 ± 1.18 kpc for the EP and very similar 3.16 ± 1.30 and 3.17 ± 0.64 kpc for the breaks and truncation sub-samples. The mean inner scalelength measured with the PAS is higher and has more scatter at 3.87 ± 1.59 kpc, with again rather similar sub-samples at 3.81 ± 1.65 and 3.95 ± 1.49 kpc. The mean inner scalelength of the ellipse-fit profiles was 3.46 ± 1.64 kpc. This is very similar to Pohlen & Trujillo (2006), who found a mean scalelength h_0 of 3.8 ± 1.2 kpc.

The same tight correlations with the ellipse-fit profiles remain for the scalelengths after the feature for both profiles. The biggest scatter increase occurs in the truncation sample of the PAS profiles, where $\rho_{\mathrm{PAS,\,truncations}} = 0.732$. This result, however, remains comfortably significant at $p < 0.005$. The mean outer scalelength h_f as measured through the EP was 2.26 ± 1.03 kpc for the EP methods. The breaks and truncations have the mean outer scalelength of 2.43 ± 1.04 kpc and 1.68 ± 0.70 kpc, respectively. For the PAS, we have found h_f = 2.13 ± 1.28 kpc, with subdivisions into 2.61 ± 1.41 and 1.36 ± 0.41 kpc. The average ellipse outer scalelength h_f is 2.12 ± 0.98 kpc, with the breaks at 2.40 ± 1.08 kpc and the truncations at 1.61 ± 0.47. The outer truncation scalelengths of the EP and ellipse-fit profiles thus tend to be longer than their PAS counterparts. In edge-on galaxies, the scalelength for a truncation is even shorter, at only 1.5 ± 0.1 kpc. The break scalelengths are similar at 2.7 ± 0.3 kpc (Martín-Navarro et al. 2012).

As we noted before, the PAS surface brightness levels are in mag arcsec^{-1} rather than mag arcsec^{-2}, making them distance dependent. As a quick test to see if the distance could be a complicating fact in the increased scatter of the PAS, we model a very simple galaxy consisting of no more than a face-on, truncated exponential disc. In these models we have put the truncations at various distances, thus changing the number of points available in the minor-axis summation. In this test, we found that the ratio between the ellipse-derived scalelengths and the PAS-derived scalelengths did change with distance, but the scatter was below 1 per cent of the derived scalelengths. Thus, distance does not affect the derived scalelengths significantly.

Table 5. Derived break colours. Break colours are given in AB mag arcsec^{-2}.

	Ellipse		EP						PAS					
Galaxy	$\mu_f\, r'$	±	$\mu_f\, r'$	±	$\mu_f\, g'$	±	$\mu_f\, i'$	±	$\mu_f\, r'$	±	$\mu_f\, g'$	±	$\mu_f\, i'$	±
IC1125	23.613	0.075	23.630	<0.001	23.971	0.001	23.025	0.001	18.822	0.077	19.301	0.033	18.978	0.034
IC1158	23.980	0.042	24.080	0.002	24.541	0.001	23.728	0.002	18.977	0.028	19.261	0.028	18.528	0.039
NGC 0450	24.061	0.029	23.899	0.001	24.169	0.001	23.766	<0.001	18.118	0.073	18.304	0.004	17.870	0.060
NGC 0941	24.798	0.074	24.684	0.006	24.911	0.005	24.959	0.004	18.834	0.072	19.440	0.040	18.306	0.046
NGC 2701	22.246	0.020	22.265	0.002	22.604	0.002	21.956	0.002	16.656	0.016	16.979	0.016	16.482	0.012
NGC 2967	24.819	0.036	24.663	0.001	25.084	0.003	24.275	0.003	19.341	0.061	19.209	0.045	18.656	0.058
NGC 3055	22.907	0.044	23.265	<0.001	23.613	0.001	23.035	0.001	18.369	0.042	19.047	0.057	17.744	0.058
NGC 3259	24.295	0.029	23.908	0.001	24.369	0.001	23.608	0.002	18.282	0.022	19.025	0.030	18.068	0.034
NGC 3423	22.941	0.031	23.066	0.001	23.463	0.002	22.913	<0.001	17.314	0.015	17.541	0.021	17.166	0.012
NGC 3589	23.177	0.029	23.096	<0.001	23.357	<0.001	22.906	<0.001	18.158	0.017	18.429	0.034	17.712	0.029
NGC 3982	24.042	0.035	23.944	0.003	24.306	0.001	23.683	0.002	17.421	0.026	17.899	0.022	17.269	0.050
NGC 4041	24.257	0.024	24.437	0.002	25.051	0.001	24.064	0.002	18.151	0.034	18.993	0.057	17.533	0.097
NGC 4102	21.618	0.015	21.853	<0.001	22.592	0.001	21.436	<0.001	16.472	0.018	17.140	0.012	16.073	0.018
NGC 4545	23.526	0.088	23.675	0.001	24.094	<0.001	23.482	<0.001	18.379	0.029	18.652	0.022	18.232	0.012
NGC 4653	26.072	0.067	24.659	0.002	25.234	0.009	24.756	0.011	18.999	0.075	19.307	0.012	18.629	0.022
NGC 4904	22.069	0.022	22.509	0.002	22.824	0.002	22.391	0.005	16.875	0.008	17.288	0.013	16.524	0.010
NGC 5147	21.211	0.007	21.410	<0.001	21.810	<0.001	21.259	0.001	16.450	0.019	16.936	0.020	16.369	0.032
NGC 5300	23.249	0.028	23.044	0.006	23.405	0.008	22.826	0.005	17.945	0.025	18.299	0.006	17.537	0.015
NGC 5334	23.976	0.051	23.735	0.002	24.139	0.001	23.448	0.001	17.308	0.042	17.501	0.048	17.378	0.011
NGC 5376	21.286	0.022	21.248	<0.001	21.838	0.001	20.895	<0.001	16.789	0.009	17.287	0.017	16.388	0.014
NGC 5430	22.893	0.079	23.359	0.001	23.656	0.005	23.007	0.002	17.348	0.013	17.610	0.016	16.948	0.016
NGC 5480	24.281	0.120	22.080	0.117	22.308	0.159			16.226	0.100	17.649	0.119	17.268	0.080
NGC 5668	23.244	0.016	23.372	0.000	23.771	0.001	22.580	0.004	17.790	0.027	17.933	0.010	17.447	0.012
NGC 5693	23.676	0.111	23.634	0.002	23.942	0.001	23.495	0.001	18.168	0.029	18.877	0.043	17.717	0.048
NGC 5774	24.649	0.118	24.527	0.001	24.812	0.006	24.516	0.002	17.893	0.014	18.524	0.045	17.832	0.020
NGC 7437	22.899	0.026	22.789	0.001	23.137	0.003	22.649	0.002	17.845	0.041	18.280	0.059	16.789	0.063
PGC006667	24.563	0.111	24.418	0.013	25.049	0.016	24.195	0.020	19.128	0.048	19.369	0.065	18.765	0.062
UGC02081	25.691	0.113	25.127	0.003	25.192	0.017	24.760	0.018	19.652	0.113	19.687	0.116	19.201	0.061
UGC06518	23.739	0.229	23.969	0.016	24.098	0.001	23.833	0.030	19.063	0.067	19.391	0.020	18.626	0.088
UGC06903	23.853	0.038	23.763	0.001	24.153	0.001	23.503	0.002	18.093	0.003	18.578	0.017	17.708	0.019
UGC07700	24.121	0.071	24.053	0.004	24.515	0.002	23.615	0.002	19.245	0.021	19.729	0.030	18.862	0.107
UGC08084	24.052	0.052	24.012	0.005	24.400	0.002	23.737	0.003	18.974	0.031	18.650	0.014	18.213	0.165
UGC08658	23.930	0.032	23.698	0.000	24.086	0.001	23.388	0.004	18.187	0.043	18.561	0.006	18.408	0.032
UGC09741	23.260	0.026	23.250	0.000	23.839	0.000	22.982	0.000	18.265	0.026	18.631	0.025	17.850	0.036
UGC09837	24.615	0.029	24.403	0.005	24.716	0.003	24.135	0.006	19.087	0.020	19.612	0.023	19.308	0.085
UGC12709	25.177	0.054	25.140	0.002	25.464	0.002	24.967	0.006	20.017	0.034	20.339	0.127	19.809	0.046

The feature radii from the ellipse-fit profiles to the feature radii measured in the other profiles for the r'-band images are also tightly correlated between the various methods. This is expected, as any other result would have caused the profile to be flagged. Again fitting this relation with a linear approximation, we find that both the EP and PAS profiles follow $h_{1,\mathrm{PASandEP}} = 1.03\, h_{\mathrm{f,ell}}$. The mean radius R_f for the EP is 8.38 ± 2.96 kpc in the whole sample. The radii R_f for the breaks and truncation sub-samples are 8.13 ± 2.77 and 9.29 ± 3.39 kpc. In comparison, the PAS profile radii R_f have a mean position of 8.32 ± 3.15 kpc, with the break and truncation sub-samples at 7.61 ± 3.02 and 9.44 ± 3.03 kpc. The EP results are similar to Pohlen & Trujillo (2006), who report a typical radius of $R_\mathrm{f} = 9.2 \pm 2.4$ kpc for their type II-CT sample and $R_\mathrm{f} = 9.5 \pm 6.5$ for their Outer Lindblad Resonance sample. An average radius of 7.9 ± 0.9 kpc was reported for the inner breaks in the edge-on sample of Martín-Navarro et al. (2012), while the average truncation was found at 14 ± 2 kpc.

Looking at the radius of the feature in terms of the number of (inner) scalelengths R_f/h_0, we have a mean of 2.84 ± 0.98 for the EP and 2.32 ± 0.75 for the PAS. This difference is a reflection of the result previously reported that PAS profiles tend to have longer inner scalelengths compared to the ellipse-fit profile and EP. The breaks and truncation sub-samples for the breaks show similar behaviour. For the EP, we find 2.83 ± 1.06 for the breaks and 2.90 ± 0.67 for the truncations. For the PAS, we find 2.20 ± 0.83 and 2.52 ± 0.57. Overall, we see that the truncations suffer from less scatter than the breaks. For truncations in edge-on galaxies, R_f/h_0 is expected to lie around 4.2 ± 0.6 (van der Kruit & Searle 1982a) or 2.9 ± 0.7 (Pohlen et al. 2000). Sixteen face-on galaxies from the sample of Wevers (1984) and Wevers, van der Kruit & Allen (1984) were analysed by van der Kruit (1988) for the presence of truncations, who found $R_\mathrm{f}/h_0 = 4.5 \pm 1.0$. Bosma & Freeman (1993) argued that a large range of radii could be found, as seven galaxies in the Wevers et al. (1984) sample have a relatively bright 'edge' at $R_\mathrm{f}/h_0 = 2.8 \pm 0.4$, while their other galaxies did not show this and would thus have $R_\mathrm{f}/h_0 > 4$. Pohlen et al. (2002) find for three galaxies a value of 3.9 ± 0.7. Pohlen & Trujillo (2006) find a far lower $R_\mathrm{f}/h_0 \sim 2.5 \pm 0.6$ for their type II-CT sample and 1.7 for their breaks sample, which, as we argue in more detail in Peters et al. (2015), is due to different definitions of what is a break and what is a truncation plus the way to mark this. There also remains the question of the consistency in measuring scalelengths in face-on galaxies and recovering these from projected data of edge-ons. In the literature, there are thus studies indicating average values of around 4 and less than 3, and we see for the moment no consensus appearing. The indicative value of 3.5–4 from figs 1 and 2 in Kregel

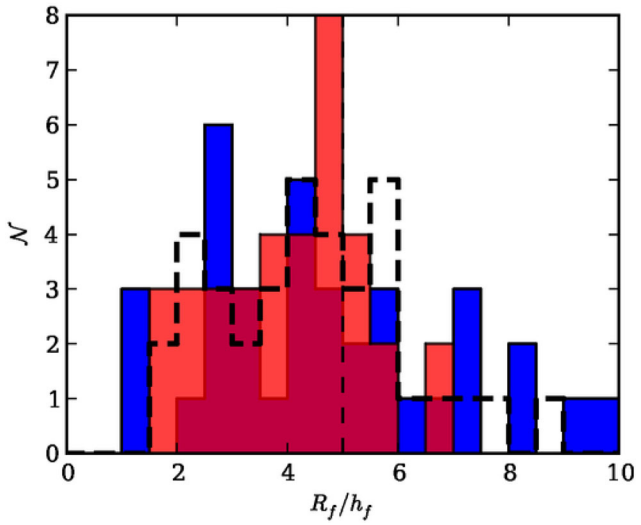

Figure 4. Histogram of R_f/h_f for the final sample. The dashed vertical line represents the $R_f/h_f = 5$ threshold proposed by Martín-Navarro et al. (2012), with all points to the left considered breaks and all points to the right considered truncations. The light-red denotes the EP, while the darker blue denotes the PAS profiles. The thick dashed profile shows the distribution of the ellipse-fit profiles.

Table 6. List of truncations based on the Martín-Navarro et al. (2012) criterion.

Galaxy	In EP?	In PAS?	Figure
IC1125	×	×	A2
IC1158		×	A3
NGC 0450	×	×	A4
NGC 0941		×	
NGC 2701	×		
NGC 3055	×	×	
NGC 3423	×	×	
NGC 4545	×	×	
NGC 4653	×	×	
NGC 5300		×	
NGC 5430		×	
PGC006667		×	
UGC08084		×	
UGC09837	×	×	
UGC12709		×	

& van der Kruit (2004) would seem in the light of this discussion not to do justice to the small values found and we revise our indicative value to 3–4.

4.4.2 *Sharpness of the breaks*

In Fig. 8, the 'sharpness' of the break is shown as measured through the ratio of inner over outer scalelengths h_0/h_b. Breaks from the EP range in strength from just above 0 until 3.5, while the PAS range up until 5. The average EP break sharpness is $h_0/h_b = 1.57 \pm 0.64$, while the PAS is at $h_0/h_b = 2.18 \pm 0.84$. This reflects the difference between face-on and edge-on profiles, where edge-on profiles typically have sharper features, going up to 12 (Martín-Navarro et al. 2012). Similar to our EP results, Pohlen & Trujillo (2006) found $h_0/h_b = 2.1 \pm 0.5$, ranging from 1.3 to 3.6, in the type II-CT sample. Our more extensive classification into type II galaxies creates the difference at the lower end of this range. Truncations and breaks

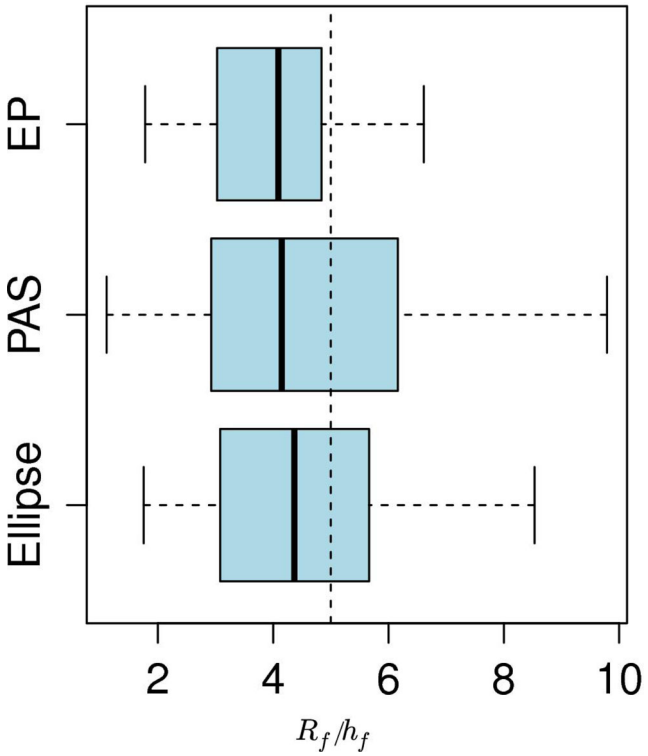

Figure 5. Boxplot of R_f/h_f for the final sample. Thick vertical stripes denote the median values, the boxes denote the outlines of the 25 and 75 per cent and the whiskers denote the minimum and maximum. The dashed vertical line represents the $R_f/h_f = 5$ threshold proposed by Martín-Navarro et al. (2012), with all points to the left considered breaks and all points to the right considered truncations.

overlap in both profile types, although the truncations tend to lie only on higher values. Compared to the EP, the PAS has a wider and more spread, and can thus reach a wider range of sharpness levels.

Fig. 8 offers an interesting alternative to the Martín-Navarro et al. (2012) classification scheme of $R_f/h_f = 5$. As can be seen from the figure, the truncations – as classified using the $R_f/h_f = 5$ in the PAS – are all at high values of h_0/h_f. There are however also galaxies that did not meet the $R_f/h_f \geq 5$ criterion, but which still have high values of h_0/h_f. An alternative scheme could therefore be to classify all galaxies as having a truncation when the sharpness of a break is above some threshold. Observing the figure, a value of $h_0/h_b = 2$ would seem appropriate, although we admit that this has a certain level of arbitrariness.

In Fig. 9, we plot the relation of h_f with R_f/h_f. There is a very clear anticorrelation between the two. Schaye (2004) predicted the presence of an anticorrelation after studying simulations of the thermal and ionization structure of the gaseous discs by Mo, Mao & White (1998). The transition to the cold interstellar medium phase is responsible for the onset of local gravitational instability, which triggers star formation. For an exponential disc, an empirical relation was found which could match the data well (equation 5). Here, M_{disc} is the total mass of the disc and Σ_c is the critical face-on surface density of the disc (Kregel & van der Kruit 2004),

$$\frac{R_f}{h_f} = \ln \frac{M_{disc}}{2\pi h_f^2 \Sigma_c}. \quad (5)$$

We apply this model to Fig. 9. The model fits the breaks sub-sample well, but fails to recover the general shape of the sample if we include the truncation sample.

Table 7. Correlation tests for the various variables. Most are self-explanatory, except possibly j, which is the specific angular momentum (see text). The ρ stands for the Spearman correlation coefficient. The null hypothesis is tested with p, where values of $p < 0.05$ indicate a (2σ) significant correlation. These have been highlighted as boldface in the table.

Variable 1	Variable 2	ρ	p	$\rho_{\rm break}$	$p_{\rm break}$	$\rho_{\rm truncation}$	$p_{\rm truncation}$
h_0 (ell)	h_0 (EP)	**0.966**	**<0.01**	**0.969**	**<0.01**	**0.952**	**<0.01**
h_0 (ell)	h_0 (PAS)	**0.874**	**<0.01**	**0.879**	**<0.01**	**0.881**	**<0.01**
$h_{\rm f}$ (ell)	$h_{\rm f}$ (EP)	**0.942**	**<0.01**	**0.925**	**<0.01**	**0.952**	**<0.01**
$h_{\rm f}$ (ell)	$h_{\rm f}$ (PAS)	**0.875**	**<0.01**	**0.927**	**<0.01**	**0.732**	**<0.01**
h_0 (ell)	Δh_0 ($g' - r'$) (PAS)	−0.11	0.53	−0.16	0.41	0.14	0.74
h_0 (ell)	Δh_0 ($r' - i'$) (PAS)	**0.496**	**<0.01**	**0.537**	**<0.01**	0.24	0.57
h_0 (ell)	Δh_0 ($g' - r'$) (PAS)	0.03	0.85	0.10	0.66	<0.01	0.99
h_0 (ell)	Δh_0 ($r' - i'$) (PAS)	0.03	0.86	0.06	0.80	−0.07	0.81
$h_{\rm f}$ (ell)	$\Delta h_{\rm f}$ ($g' - r'$) (EP)	0.22	0.20	0.19	0.33	0.33	0.42
$h_{\rm f}$ (ell)	$\Delta h_{\rm f}$ ($r' - i'$) (EP)	−0.31	0.07	−0.20	0.32	−0.38	0.35
$h_{\rm f}$ (ell)	$\Delta h_{\rm f}$ ($g' - r'$) (EP)	0.23	0.18	0.40	0.06	−0.18	0.53
$h_{\rm f}$ (ell)	$\Delta h_{\rm f}$ ($r' - i'$) (EP)	−0.15	0.38	−0.18	0.43	0.29	0.31
$R_{\rm f}$ (ell)	$R_{\rm f}$ (EP)	**0.977**	**<0.01**	**0.973**	**<0.01**	**0.952**	**<0.01**
$R_{\rm f}$ (ell)	$R_{\rm f}$ (PAS)	**0.936**	**<0.01**	**0.878**	**<0.01**	**0.960**	**<0.01**
$\mu_{r'}$ (EP)	$\mu_{g'-r'}$ (EP)	−0.07	0.71	−0.15	0.46	0.29	0.49
$\mu_{r'}$ (EP)	$\mu_{r'-i'}$ (EP)	−0.05	0.77	−0.02	0.92	−0.24	0.57
$\mu_{r'}$ (PAS)	$\mu_{g'-r'}$ (PAS)	−0.26	0.13	−0.34	0.13	0.17	0.55
$\mu_{r'}$ (PAS)	$\mu_{r'-i'}$ (PAS)	0.30	0.08	**0.487**	**0.02**	−0.09	0.75
$\mu_{g'-r'}$ (EP)	$v_{\rm rot}$	**0.359**	**0.03**	0.37	0.05	0.19	0.65
$\mu_{g'-r'}$ (PAS)	$v_{\rm rot}$	0.19	0.25	0.27	0.23	0.13	0.65
$\mu_{g'-r'}$ (EP)	$M_{\rm B,abs}$	−0.14	0.43	−0.13	0.52	−0.21	0.61
$\mu_{g'-r'}$ (PAS)	$M_{\rm B,abs}$	−0.08	0.64	−0.13	0.56	−0.06	0.84
$\mu_{r'}$ (EP)	$v_{\rm rot}$	−0.15	0.38	−0.22	0.26	0.26	0.53
$\mu_{r'}$ (PAS)	$v_{\rm rot}$	−0.31	0.07	−0.38	0.08	−0.13	0.67
$\mu_{r'}$ (EP)	$M_{\rm B,abs}$	0.09	0.58	0.12	0.55	0.33	0.42
$\mu_{r'}$ (PAS)	$M_{\rm B,abs}$	0.21	0.22	0.34	0.13	0.40	0.15
$R_{\rm f}$ (EP)	$v_{\rm rot}$	0.03	0.87	−0.04	0.84	0.36	0.39
$R_{\rm f}$ (PAS)	$v_{\rm rot}$	0.04	0.82	−0.02	0.93	0.34	0.24
$R_{\rm f}$ (EP)	$M_{\rm B,abs}$	−0.19	0.26	−0.12	0.53	−0.10	0.82
$R_{\rm f}$ (PAS)	$M_{\rm B,abs}$	−0.17	0.32	−0.12	0.59	−0.10	0.74
$R_{\rm f}$ (EP)	j	0.03	0.87	−0.04	0.84	0.36	0.39
$R_{\rm f}$ (PAS)	j	0.04	0.82	−0.02	0.93	0.34	0.24
a/b	h_0 (EP)	0.06	0.75	0.14	0.48	−0.44	0.27
a/b	h_0 (PAS)	0.07	0.70	0.26	0.25	−0.34	0.23
a/b	$h_{\rm f}$ (EP)	−0.26	0.12	−0.23	0.24	−0.16	0.71
a/b	$h_{\rm f}$ (PAS)	**−0.404**	**0.01**	−0.22	0.33	−0.49	0.08
a/b	$R_{\rm f}/h_{\rm f}$ (EP)	0.30	0.08	0.35	0.07	0.31	0.45
a/b	$R_{\rm f}/h_{\rm f}$ (PAS)	**0.349**	**0.04**	0.37	0.09	0.36	0.20
a/b	$h_0/h_{\rm f}$ (EP)	0.22	0.20	0.28	0.15	−0.01	0.98
a/b	$h_0/h_{\rm f}$ (PAS)	0.32	0.06	0.35	0.11	0.06	0.85
$R_{\rm f}$ (EP)	$\mu_{g'-r'}$ (EP)	0.10	0.57	−0.01	0.97	0.62	0.10
$R_{\rm f}$ (EP)	$\mu_{r'-i'}$ (EP)	0.21	0.23	0.30	0.13	−0.12	0.78
$R_{\rm f}$ (PAS)	$\mu_{g'-r'}$ (PAS)	**−0.349**	**0.04**	−0.35	0.11	0.09	0.75
$R_{\rm f}$ (PAS)	$\mu_{r'-i'}$ (PAS)	0.05	0.79	0.20	0.37	−0.10	0.73
$h_{\rm f}$ (EP)	$R_{\rm f}/h_{\rm f}$ (EP)	**−0.515**	**<0.01**	**−0.449**	**0.02**	−0.17	0.69
$h_{\rm f}$ (PAS)	$R_{\rm f}/h_{\rm f}$ (PAS)	**−0.632**	**<0.01**	**−0.441**	**0.04**	−0.37	0.19

4.4.3 Variations per band

It is interesting to test for variations of the scalelengths as measured in different bands. We test this by performing a correlation test of the ellipse-fit scalelengths h_0 and $h_{\rm f}$ with the differences of the scalelengths measured in two different bands Δh_0 and $\Delta h_{\rm f}$. So e.g. $\Delta h_0(g' - r')$(PAS) is the difference in scalelength h_0 measured in g' and r' using the PAS method. The results from these tests are shown in Table 7 (lines 5–12). Only one statistically significant correlation is found. The difference of the inner scalelengths measured with the PAS in the r' and i' bands has a correlation of $\rho = 0.50$ at $p < 0.005$. We demonstrate this correlation in Fig. 10. The points that lead to this correlation are mostly points with high uncertainty, and we thus remain sceptical about any actual correlation.

The differences in brightness between bands at the features from both methods are compared in Table 8. If the error bars are included in the comparison, the brightness differences between bands are practically the same, regardless of the use of either the EP or PAS. The one potential exception to this can be seen in the $r' - i'$ truncation sample, where for the EP we have 0.19 ± 0.13 and for the PAS 0.30 ± 0.20. As demonstrated earlier, the EP is particularly sensitive to background noise. Out of all bands, the i' has the highest background noise, so most likely the offset is due

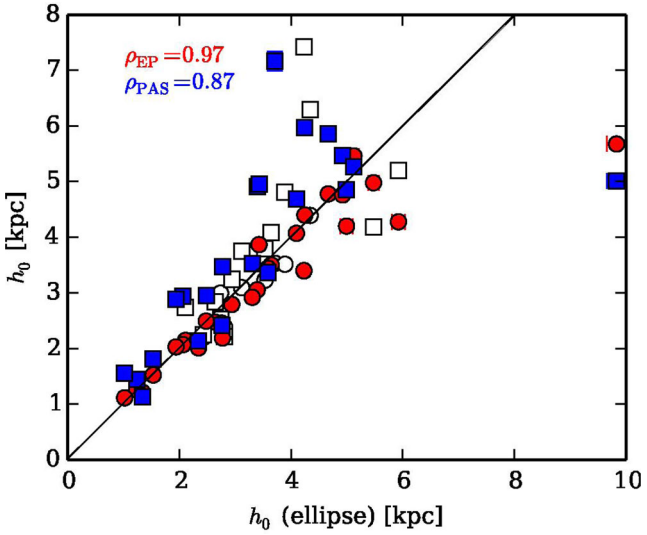

Figure 6. The inner scalelength of the linear fits to the r'-band profile, h_0, compared to the scalelengths as derived from the ellipse-fit profiles. The circles denote the EP and the squares denote the PAS profiles. Filled markers are breaks, while open markers are likely truncations. The correlation significance p is also shown.

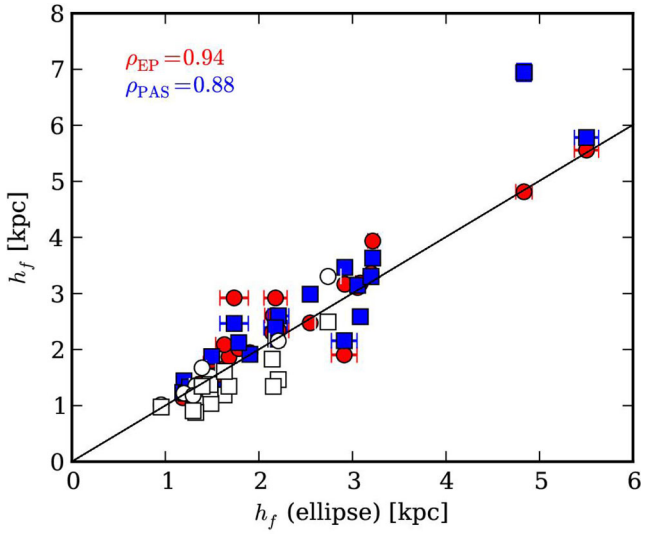

Figure 7. The outer scalelength of the linear fits to the r'-band profile, h_f, compared to the scalelengths as derived from the ellipse-fit profiles. The circles denote the EP and the squares denote the PAS profiles. Filled markers are breaks, while open markers are likely truncations. The correlation significance p is also shown.

to sampling of the background. We have also tested any potential correlation of feature radius R_f as measured by the EP or PAS profiles, with the brightness differences $g' - r'$ and $r' - i'$. We find a weak correlation of $\rho = -0.35$ and significance $p = 0.04$ in the PAS $g' - r'$ full data set sample, which we show in Fig. 11. This correlation is likely due to measurement errors of a couple of bad points at the outskirts.

The r'-band magnitude at the feature has also been compared to the $\Delta\mu(r' - g')$ and $\Delta\mu(r' - i')$ values. The rank correlation tests show that there is no strong correlation for r' with $\Delta\mu(r' - g')$ and $\Delta\mu(r' - i')$, with the maximum at only $\rho = 0.30$ and $p = 0.08$.

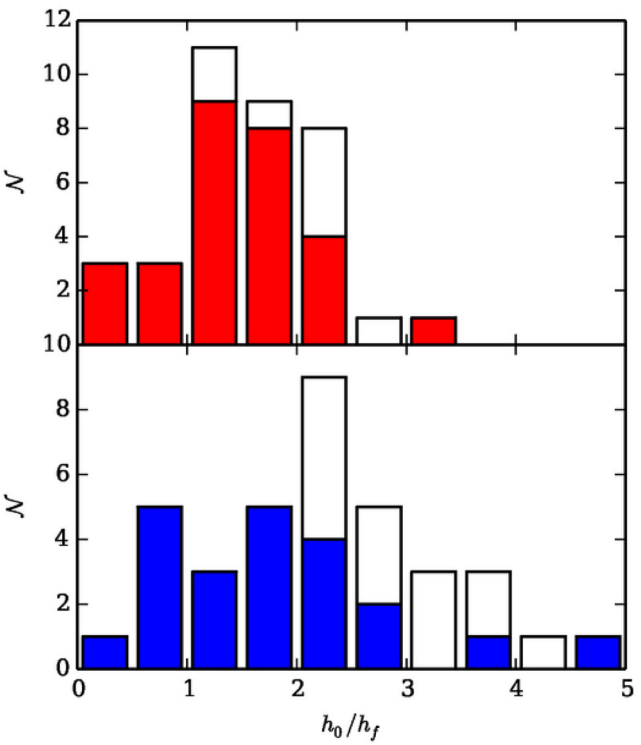

Figure 8. Histogram of h_0/h_f for the final sample. In the top plot, the results are shown for the EP. Filled red bars are the breaks. Stacked on top of those are the white bars for the truncations. The bottom panel features the results for the PAS profiles, in blue the breaks and in white the truncations.

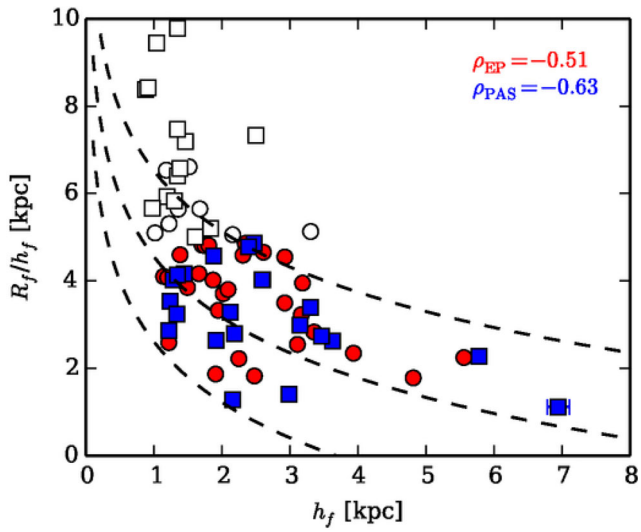

Figure 9. Scalelength h_f with ratio R_f/h_f. Filled markers are breaks, open markers are truncations. The top panel shows the results for the PAS and the bottom panel for the EP. Dashed black lines represent the empirical scaling relations from Schaye (2004), using $\Sigma_0 = 5.9$ M$_\odot$ pc^2 and M_{disc} as 5×10^8, 3.5×10^9 and 25×10^9 M$_\odot$.

The only exception is for the PAS profiles from the $r' - i'$ breaks sub-sample, where there is a correlation of $\rho = 0.49$ and $p = 0.02$. This correlation is due to the same points as the correlation of h_0 with $\Delta h_0(r' - i'0)$ in the PAS.

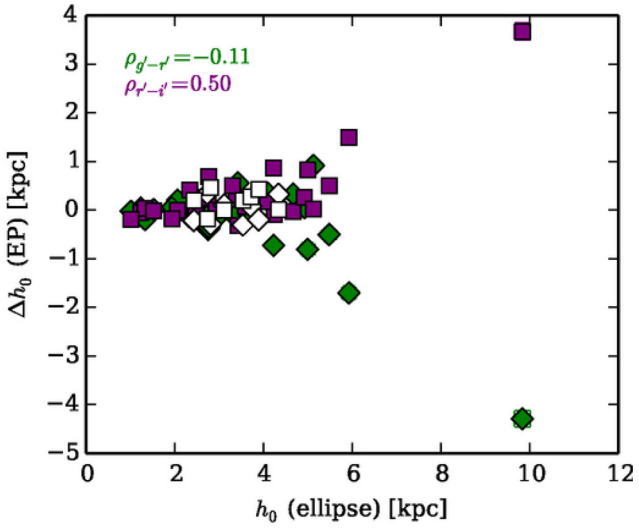

Figure 10. Correlations for differences in scalelength h_0 per band as measured using the EP, with the scalelength from the r'-band ellipse-fit profiles. The corresponding significance values are superimposed on the panel. Diamond-shaped boxes represent the $g' - r'$ points, square boxes represent the $r' - i'$. Filled markers are breaks, open markers are truncations.

Table 8. Average brightness differences at the feature radius between various bands.

Band and method	Full sample	Breaks	Truncations
$\Delta\mu(g' - r')$ (EP)	0.38 ± 0.14	0.38 ± 0.15	0.39 ± 0.09
$\Delta\mu(g' - r')$ (PAS)	0.41 ± 0.29	0.46 ± 0.31	0.32 ± 0.23
$\Delta\mu(r' - i')$ (EP)	0.25 ± 0.18	0.27 ± 0.19	0.19 ± 0.13
$\Delta\mu(r' - i')$ (PAS)	0.29 ± 0.34	0.28 ± 0.39	0.30 ± 0.20

4.4.4 Correlations with absolute magnitude, maximum rotation and specific angular momentum

Martín-Navarro et al. (2012) found that the truncation radius of a galaxy is strongly correlated with the maximum rotational velocity $v_{\rm rot}$ of a galaxy, having a correlation of $\rho_{\rm truncation} = 0.81$. The breaks in their sample were correlated at only $\rho_{\rm break} = 0.50$. In contrast, Pohlen & Trujillo (2006) report no correlation with rotation. They do report a weak correlation of the brightness at the feature $\mu_{r'}$ with the absolute magnitude $M_{\rm B,abs}$. We explore possible correlations of the feature radii $R_{\rm f}$, surface brightness at the feature μ and differences in brightness between bands at the feature $\mu\Delta$ with absolute magnitude $M_{\rm abs}$ and maximum rotation $v_{\rm rot}$ in Table 7. We find only one weak correlation in the difference between the g' and r' surface brightness at the feature radius, as measured with the EP method, with the rotation velocity $v_{\rm rot}$. The correlation strength is $\rho = 0.36$ and $p = 0.03$.

Martín-Navarro et al. (2012) also perform a correlation test of the break and truncation radii with the specific angular momentum j, calculated using the empirical expression by Navarro & Steinmetz (2000),[4]

$$j \approx 1.3 \times 10^3 \left[\frac{v_{\rm rot}}{200\,{\rm km\ s^{-1}}}\right]^2 {\rm km\ s^{-1} h^{-1} kpc}. \quad (6)$$

As this is a rescaling of $v_{\rm rot}$, the correlation remains the same. They find that the feature radius only correlates well beyond

[4] In this paper, we adopt $h = 0.7$.

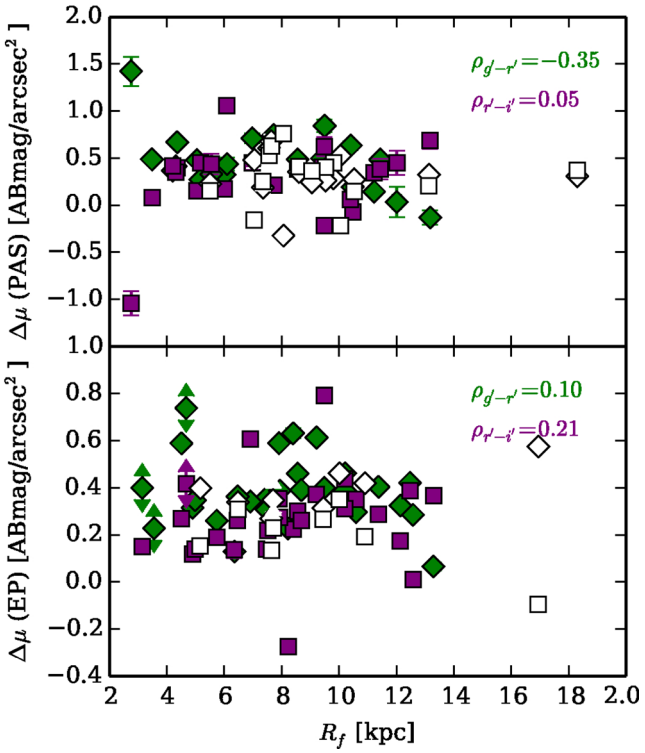

Figure 11. Correlations of the break radius $R_{\rm f}$, for each method, with the difference in brightness for various bands. Shown are $g' - r'$ (diamond markers) and $r' - i'$ (box markers). Filled markers are breaks, open markers are truncations. The top panel shows the results for the PAS and the bottom panel for the EP.

$r_{\rm b} = 8$ kpc. For a smaller disc with $v_{\rm rot} < 100\,{\rm km s^{-1}}$, $r_{\rm break}$ and $v_{\rm rot}$ are essentially unlinked. When examining the full radii range, we also do not find a statistically significant correlation. The same holds when limiting ourselves to all features beyond $r > 8$.

4.4.5 Effect of inclination

In Section 4.4.2, we found that the PAS profiles typically tend to have sharper breaks than the ellipse-fit profiles and EP. As the PAS projects data as if it was edge-on, it is also interesting to compare the effect of inclinations in this. To this end, we have tested the correlation of a/b (major axis over minor axis) with scalelengths h_0 and $h_{\rm f}$, $h_0/h_{\rm f}$ and $R_{\rm f}/h_{\rm f}$, in Table 7. The results are also visualized in Fig. 12.

We find no significant correlation between a/b and inner scalelength h_0. There may be a negative trend visible in the truncation-only sample, as both the EP and PAS profiles have reasonably strong correlations with $\rho = -0.44$ and $\rho = -0.34$, but more point will be required before this is significant. When looking at the outer scalelength, a negative correlation of $\rho = -0.40$ at $p = 0.01$ is found for the PAS. This correlation is mostly due to the truncation sample, which has $\rho = -0.49$ at $p = 0.08$, which is also clear from the figure. Thus, the PAS outer scalelength typically gets shorter with higher inclination, while the inner scalelengths barely depend on inclination.

The $R_{\rm f}/h_{\rm f}$ has a weak but significant correlation with a/b in the PAS method, $\rho = 0.35$ at $p = 0.04$, a correlation which holds (albeit insignificantly) for both subsets. Interestingly, the EP results follow similar correlations, although those are not significant. The

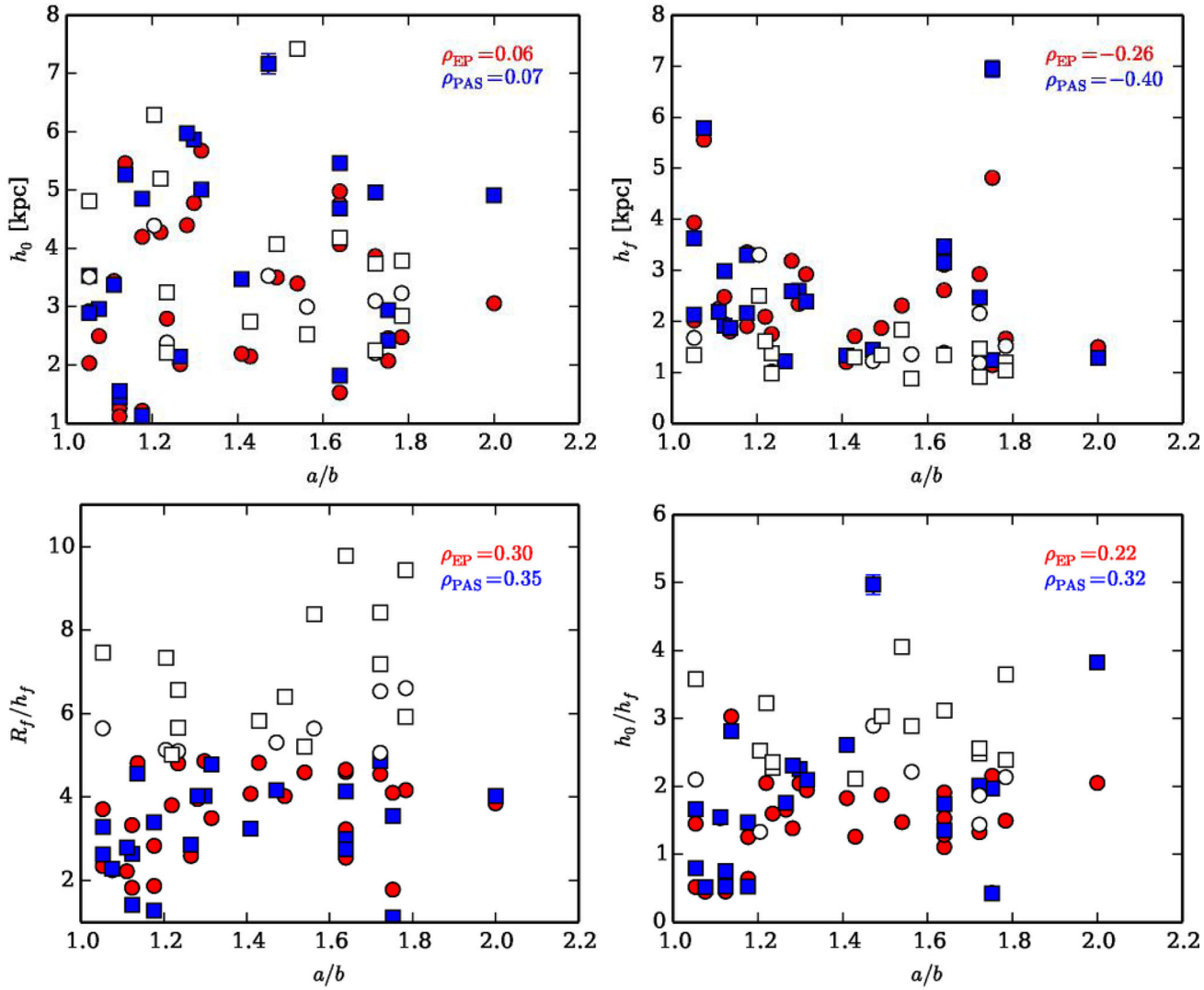

Figure 12. Correlation of various parameters with inclination (expressed as a/b). Top row shows with scalelength h_0 (left) and h_f (right). Bottom row has the h_0/h_f (right) and R_f/h_f (left) correlations. The statistical correlation tests are plotted in each panel. Boxes represent the PAS points, while circles represent the EP points. Open markers represent truncations, while filled markers represent boxes.

sharpness of the breaks h_0/h_f has no significant correlation with a/b in either method.

5 CLOSING DISCUSSION AND CONCLUSIONS

We have developed two new approaches for extracting the surface photometry of a face-on galaxy. The EP work under the assumption that the surface brightness of a galaxy decreases as the radius increases. By starting with the brightest pixel and moving to lower brightness levels, each level can be assigned an equivalent area ellipse containing the surface of all pixels that are at or brighter than that level. The equivalent ellipse then gives the equivalent radius. The other method is the PAS, which works by summing the light on to the principal axis of the galaxy. This method then gives the equivalent of the profile as if the galaxy was seen edge-on. We have then tested this method on a sub-sample of the galaxies from Pohlen & Trujillo (2006).

Seen overall, we find that both our methods perform well. Considering the fundamentally different method used to derive them, a detailed comparison that we have made (not illustrated) shows to us that the EP are remarkably similar to the ellipse-fit profiles as measured by Pohlen & Trujillo (2006). We also point out that the classical method of elliptical averaging compares very well with results of EP, (van der Kruit 1979). There are some differences. The ellipse-fit profiles have the ability to measure local upturns in the profiles, for example due to a local bar or ring feature. By design, the EP are unable to cope with this. This can lead to slightly different scalelengths. Beyond such a bump, however, the EP and ellipse-fit profiles join up again, as for example in Fig. A1. Overall, we see that the EP behave worse at lower brightness levels than the ellipse-fit profiles. For practical purposes, the ellipse therefore remains the preferred method.

The PAS method turns out to be a very interesting approach. Compared to the EP, breaks and truncations often look sharper. A good example of this can be seen in galaxy IC1158, seen in Fig. A3, where the PAS profiles start to drop quite rapidly beyond ∼65 arcsec, much stronger than the ellipse-fit profiles. We find that the inner scalelength as measured with the PAS is on average 10 per cent longer than the same scalelength in either of the other methods. We also find a negative correlation with the inclination

as expressed by the ratio a/b. As the inclination increases, the outer scalelength of the PAS profiles gets smaller. This leads to sharper breaks h_0/h_f than are seen in ellipse-fit profiles or in the EP. Although beyond the scope of this project, it would be interesting to test if h_0/h_f, rather than R_b/h_f, is a good way to distinguish between breaks and truncations.

In edge-on galaxies, there is a well-observed correlation of the radius of the truncations with the maximum rotation velocity v_{rot} (van der Kruit 2008). This was confirmed by Martín-Navarro et al. (2012), who also found a correlation with the absolute magnitude of the galaxy $M_{B,abs}$. Various studies of face-on samples, starting with Pohlen & Trujillo (2006) and more recently for example (Muñoz-Mateos et al. 2013), have looked for and sometimes reported similar relations (e.g. their fig. 8), but in those cases it is not clear that the break radii used are referring to the equivalent features of edge-on truncations. We do not find any correlation of the surface brightness at the feature, difference in brightness between various bands at the feature, and the feature radius, with the absolute brightness $M_{B,abs}$ nor with the maximum rotation v_{rot}. Martín-Navarro et al. (2012) divide their samples up into truncations and breaks based on the criterion $R_f/h_0 = 5$, with the galaxy belonging to breaks if the ratio was below 5 and truncations if it was above it. We have split our sample into these two subsets using the same criterion and have inspected the data for correlations. We do not reproduce these correlations. We are therefore sceptical of the galaxies in our truncation sub-sample constituting true truncations in the edge-on sense. It is more likely that we are still only observing breaks. Truncations can likely only be found by using deeper imaging, such as that used by Bakos & Trujillo (2012). We will explore the use of deeper imaging to detect truncations further in Peters et al. (2016).

ACKNOWLEDGEMENTS

We thank Michael Pohlen for providing his data on the sample in electronic form.

SPCP is grateful to the Space Telescope Science Institute, Baltimore, USA, the Research School for Astronomy and Astrophysics, Australian National University, Canberra, Australia, and the Instituto de Astrofisica de Canarias, La Laguna, Tenerife, Spain, for hospitality and support during short and extended working visits in the course of his PhD thesis research. He thanks Roelof de Jong and Ron Allen for help and support during an earlier period as a visiting student at Johns Hopkins University and the Physics and Astronomy Department, Krieger School of Arts and Sciences for this appointment.

PCK thanks the directors of these same institutions and his local hosts Ron Allen, Ken Freeman and Johan Knapen for hospitality and support during many work visits over the years, of which most were directly or indirectly related to the research presented in this series of papers.

Work visits by SPCP and PCK have been supported by an annual grant from the Faculty of Mathematics and Natural Sciences of the University of Groningen to PCK accompanying of his distinguished Jacobus C. Kapteyn professorhip and by the Leids Kerkhoven-Bosscha Fonds. PCK's work visits were also supported by an annual grant from the Area of Exact Sciences of the Netherlands Organisation for Scientific Research (NWO) in compensation for his membership of its Board.

REFERENCES

Abazajian K. et al., 2004, AJ, 128, 502
Abazajian K. N. et al., 2009, ApJS, 182, 543
Bakos J., Trujillo I., 2012, preprint (arXiv:1204.3082)
Bakos J., Trujillo I., Pohlen M., 2008, ApJ, 683, L103
Bosma A., Freeman K. C., 1993, AJ, 106, 1394
Busko I. C., 1996, in Jacoby G. H., Barnes J., eds, ASP Conf. Ser. Vol. 101, Astronomical Data Analysis Software and Systems V. Astron. Soc. Pac., San Francisco, p. 139
Comerón S. et al., 2012, ApJ, 759, 98
de Vaucouleurs G., 1948, Ann. Astrophys., 11, 247
de Vaucouleurs G., 1959, Handbuch Phys., 53, 311
Elmegreen B. G., Hunter D. A., 2006, ApJ, 636, 712
Erwin P., Beckman J. E., Pohlen M., 2005, ApJ, 626, L81
Erwin P., Pohlen M., Beckman J. E., 2008, AJ, 135, 20
Freeman K. C., 1970, ApJ, 160, 811
Gutiérrez L., Erwin P., Aladro R., Beckman J. E., 2011, AJ, 142, 145
Herrmann K. A., Hunter D. A., Elmegreen B. G., 2013, AJ, 146, 104
Herrmann K. A., Hunter D. A., Elmegreen B. G., 2016, AJ, 151, 145
Jacob J. C. et al., 2010, Astrophysics Source Code Library, record ascl:1010.036
Jedrzejewski R. I., 1987, MNRAS, 226, 747
Jones C. K., Whittall K. P., MacKay A. L., 2003, Magn. Reson. Med., 50, 206
Knapen J. H., van der Kruit P. C., 1991, A&A, 248, 57
Kregel M., van der Kruit P. C., 2004, MNRAS, 355, 143
Laine J. et al., 2014, MNRAS, 441, 1992
Lang D., Hogg D. W., Mierle K., Blanton M., Roweis S., 2010, AJ, 137, 1782
Martín-Navarro I. et al., 2012, MNRAS, 427, 1102
Mo H. J., Mao S., White S. D. M., 1998, MNRAS, 295, 319
Muñoz-Mateos J. C. et al., 2013, ApJ, 771, 59
Navarro J. F., Steinmetz M., 2000, ApJ, 538, 477
Patterson F. S., 1940, Harv. Coll. Obs. Bull., 914, 9
Peters S. P. C., van der Kruit P. C., Knapen J. H., Trujillo I., Fliri J., Cisternas M., Kelvin L. S., 2016, MNRAS, in press
Pohlen M., Trujillo I., 2006, A&A, 454, 759
Pohlen M., Dettmar R.-J., Lütticke R., 2000, A&A, 357, L1
Pohlen M., Dettmar R.-J., Lütticke R., Aronica G., 2002, A&A, 392, 807
Pohlen M., Balcells M., Lütticke R., Dettmar R.-J., 2004, A&A, 422, 465
Pohlen M., Zaroubi S., Peletier R., Dettmar R.-J., 2007, MNRAS, 378, 594
Schaye J., 2004, ApJ, 609, 667
van der Kruit P. C., 1979, A&AS, 38, 15
van der Kruit P. C., 1988, A&A, 192, 117
van der Kruit P. C., 2008, in Funes J. G., Corsini E. M., eds, ASP Conf. Ser. Vol. 396, Formation and Evolution of Galaxy Disks. Astron. Soc. Pac., San Francisco, p. 173
van der Kruit P. C., Freeman K. C., 2011, ARA&A, 49, 301
van der Kruit P. C., Searle L., 1981a, A&A, 95, 105
van der Kruit P. C., Searle L., 1981b, A&A, 95, 116
van der Kruit P. C., Searle L., 1982a, A&A, 110, 61
van der Kruit P. C., Searle L., 1982b, A&A, 110, 79
Wevers B. M. H. R., 1984, PhD thesis, Univ. Groningen
Wevers B. M. H. W., van der Kruit P. C., Allen R. J., 1984, A&AS, 66, 505

SUPPORTING INFORMATION

Additional Supporting Information may be found in the online version of this article:

Appendix A. Plots for individual galaxies.
(http://www.mnras.oxfordjournals.org/lookup/suppl/doi:10.1093/mnras/stw2404/-/DC1).

Please note: Oxford University Press is not responsible for the content or functionality of any supporting materials supplied by the authors. Any queries (other than missing material) should be directed to the corresponding author for the article.

This paper has been typeset from a TEX/LATEX file prepared by the author.